FCU ePaper

逢甲大學學生報告 ePaper

報告題名：

用於對稱超級電容器之氧化鈷奈米線化學合成

Chemical synthesis of Co_3O_4 nanowires for symmetric supercapacitor device

作者：鍾孟君

系級：材料三甲

學號：D0593704

開課老師：駱榮富

課程名稱：專題討論

開課系所：材料科學與工程學系

開課學年： 107 學年度 第 2 學期

中文摘要

超級電容因其功率密度高於其他能量儲存設備，例如：鋰離子電池，所以適用在各種需要高功率突發的應用上，然其能量密度低於鋰離子電池與燃料電池等儲能器，因而限制了其實際應用之可能性。為了能簡化且實際探討超級電容之應用，本研究利用簡單的化學浴沉積法於基材上成長具有高理論電容、低成本、良好的氧化還原能力以及對環境友善性的四氧化三鈷奈米線。此外，也會針對此奈米異質結構進行分析相關的材料特性及電化學特性。

本研究結果四氧化三鈷奈米線具有 66.33 mg^{-1} 的高比表面積，此結構有利於電解質離子的嵌入和電子傳輸，高比表面機提供了更多電荷儲存。以及掃描速率 5 mVs^{-1} 下 850 Fg^{-1} 的優異比電容值，且超過 5000 次循環時電容保留率 86%的長期循環穩定性。且基板的選擇避免了黏合劑造成的界面缺陷、生長不均。

關鍵字：化學浴沉積法、奈米氧化鈷、超級電容器、對稱型超級電容器

Abstract

Because of its higher power density than other energy storage devices, such as lithium-ion batteries, supercapacitors are suitable for applications requiring high power bursts, but their energy density is lower than that of lithium-ion batteries and fuel cells. Limits the possibility of its practical application. In order to simplify and practically explore the application of supercapacitors, this study used a simple chemical bath deposition method to grow a high theoretical volume, low cost, good redox capacity and environmentally friendly cobalt trioxide nanowire on the substrate. In addition, the material properties and electrochemical properties associated with this nanostructure are also analyzed.

The results of this study have a high specific surface area of 66.33 mg-1, which is beneficial to the insertion and electron transport of electrolyte ions, and the high specific surface machine provides more charge storage. And the excellent specific capacitance value of 850 Fg-1 at a scan rate of 5 mVs-1, and the long-term cycle stability of the capacitor retention rate of 86% over 5000 cycles. Moreover, the selection of the substrate avoids interface defects and uneven growth caused by the adhesive.

Keyword：Chemical bath deposition(CBD)、Co_3O_4、Co_3O_4 nanowires、Symmetric supercapacitor

目　次

第一章 緒論

伴隨著科技演進的同時，化石能源卻逐漸邁向枯竭，因此關於能源的產生、轉換與儲存逐漸成為了大家所關注的議題。其中，由於電動汽機車、油電混合汽車與可攜帶式電子式設備的發展與普及，進而使得能量的儲存的研究更受到大家所關注[1]。在這部分的研究中又以超級電容具備有高功率密度、快速充電能力與高循環壽命，進而引起眾多學者的關注與研究[2]。超級電容根據電荷儲存機制，可分為兩種，一種為電雙層，通常使用碳基材在電極與電解質的界面累積靜電荷；另一種為擬電容，利用過度金屬氧化物或導電高分子作為電極材料，並藉由法拉第氧化還原反應儲存電荷[3]，此為在發展高性能超級電容器時，作為尋找合適的材料需要特別以此做為考量之基準。目前在超級電容的發展上常使用之金屬氧化物有二氧化釕、二氧化錳、氧化鎳、氧化鈷等，在這眾多的金屬氧化物奈米結構當中又以四氧化三鈷奈米線最為受到矚目之一，此結構具有高的比表面積、大量的邊緣、高結晶度且存在有空位缺陷，進而使其具備有良好的比電容特性[1, 4]。

綜合上述原因，為因應能源資源匱乏的世代，本實驗選擇多項研究數據顯示深具前景的四氧化三鈷作為超級電容應用之研究與深入進行探討[5, 6]。

第二章 文獻回顧

2.1 超級電容器

由電解液、集電器和電極材料組成的超級電容器，其性能與電極材料的特性有關，一般電極材料的選用為高比表面機或良好的氧化還原特性。而依據除能機制的不同，超級電容器可分為：

(1). 電雙層電容器：電解質中的正負離子於電極和電解液之間的介面定向排列，形成電容。充電時，正負離子分別往正負極移動，於電極表面形成雙電層，電極依靠靜電荷吸附正負離子。常用材料為高比表面機的碳材料。

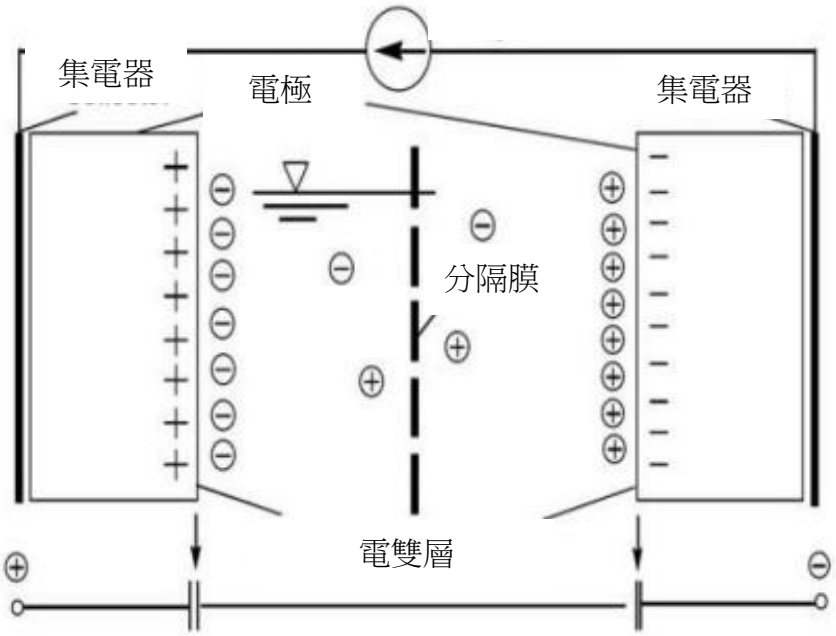

圖 2-1、電雙層儲能機制圖

(2). 擬電容：利用活性電極，例如金屬氧化物或導電高分子，進行氧化還原反應，由於氧化還原反應遵循法拉第定律，即電流質與化學反應當輛成正比，因此

又稱作法拉第電容。當外部施加電流時，電極材料快速吸附正負電解液離子，達到儲能的功用。[7]

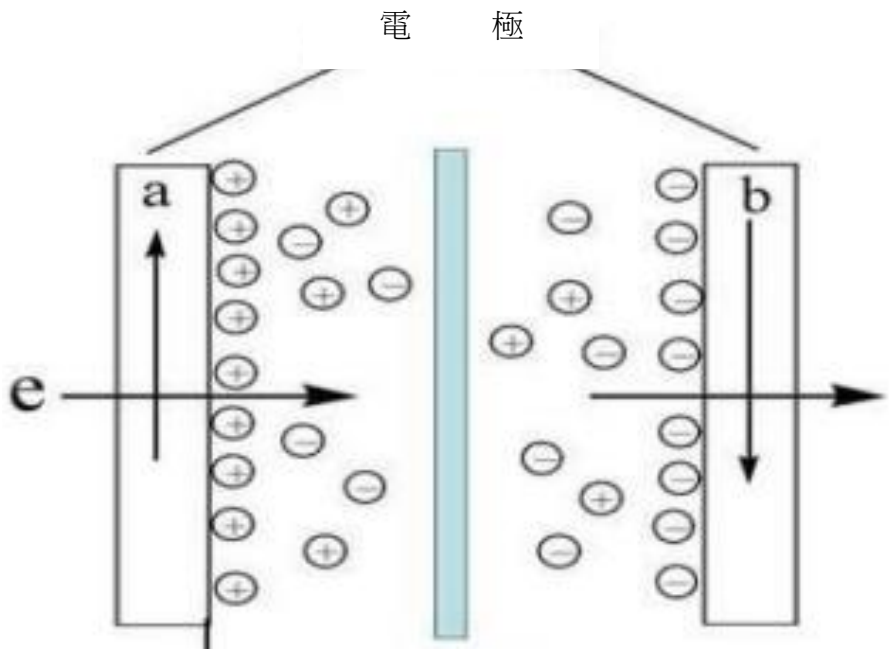

圖 2-2、擬電容儲能機制圖

2.2 四氧化三鈷奈米線

四氧化三鈷是一種非常重要的過渡金屬氧化物，目前廣泛應用於鋰電池、氣體感測器、電致變色裝置與超級電容器等[8]。在四氧化三鈷奈米結構當中又以奈米線因其平均直徑小約 70 nm 及較長的長度 25 μm，使其具備有較高的比表面積，進而使其具有顯著的擬電容特性。此外，由於此一維結構也為離子提供快速擴散的路徑，並促使四氧化三鈷奈米線與電解質界面上的電子與離子的轉移，因而使其分別在 2 Ag^{-1}與 40 Ag^{-1}時具有 754 Fg^{-1}與 610 Fg^{-1}高的比電容量，並呈現更出色的循環穩定特性[6]。

用於對稱超級電容器之氧化鈷奈米線化學合成

2.3 化學浴沉積法（Chemical Bath Deposition, CBD）

化學浴沉積法常用於製備四氧化三鈷薄膜，與其他薄膜製備的方式相比，化學浴沉積法不需要昂貴的真空設備、反應溫度低、設備簡單只需要加熱板與攪拌棒、成本低、可生長大面積薄膜，且薄膜品質與真空鍍膜的品質相差不多，因此同時也是 CdTe 太陽能電池的重要生產步驟。化學浴沉積法製備四氧化三鈷薄膜的合成機制如下：

$Co(NH_2)_2 + 6H_2O \rightarrow 4NH_8 + 6CH_2O$

$2Co^+ + 4OH^- \rightarrow 2Co(OH)_2 \downarrow$

沉積的 $Co(OH)_2$ 進一步退火為 Co_3O_4[9]

2.4 循環伏安法（CV）

循環伏安法經常被用於表現儲電裝置的性能，例如：超級電容、鋰離子電池、燃料電池等。在操作時，電極通常浸於電解液中，並在電極施加電壓，該電壓會隨時間呈現週期性變化，並同時會得到的電流，最終得到電壓與電流圖，後續透過電流相對於時間的積分可以得到累積在電極表面的電荷，進而評估其比電容量[10]。

2.5 比表面積與孔隙度分析-BET(Brunner-Emmett-Teller)

BET 用於測定多孔固體材料之比表面積與孔隙度。此項檢測能夠幫助判定材料結構與其特性之關聯，譬如孔隙度大小攸關感測器、超級電容之特性。

BET 原理為透過吸附非反應性氣體，通常為氮氣，測定已知的吸附質截面積來推定表面比表面積與孔隙度，如圖 2-3 所示。但是以壓力函數表示的吸附取線往

往不會是線性曲線，因此必須透過適當的數學方程式來推估。

$$\frac{1}{X[(\frac{P_0}{P})-1]}=\frac{1}{X_mC}-\frac{C-1}{X_mC}(\frac{P}{P_0})$$

BET 有六種典型的恆溫吸附曲線，如下圖

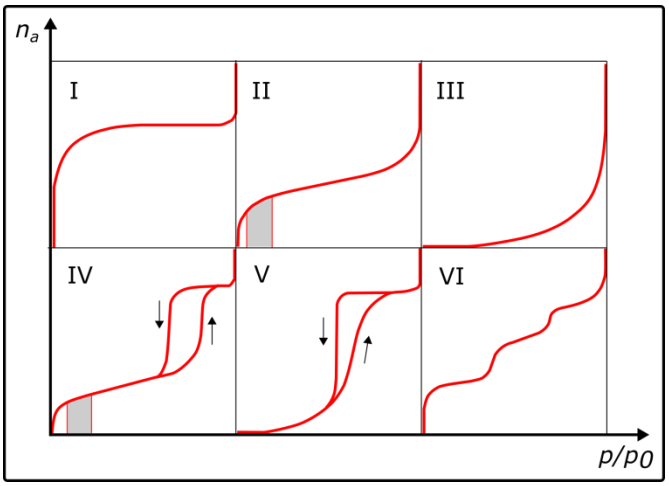

圖 2-3、IUPAC 分類的六種吸附曲線

I 型等溫線在較低的相對壓力下吸附量迅速上升，達到一定相對壓力後吸附出現飽和值。一般往往反映的是微孔填充現象，飽和吸附值等於微孔的填充體積。

II 型等溫線反映非孔性或者大孔吸附劑上典型的物理吸附過程，這是 BET 公式最常說明的對象。由於吸附質於表面存在較強的相互作用，在較低的相對壓力下吸附量迅速上升，曲線上凸。隨相對壓力的繼續增加，多層吸附逐步形成，達到飽和蒸汽壓時，吸附層無窮多，導致試驗難以測定準確的極限平衡吸附值。

III 型等溫線十分少見。吸附氣體量隨組分分壓增加而上升。曲線下凹是因為吸附質分子間的相互作用比吸附質於吸附劑之間的強，第一層的吸附熱比吸附質的液化熱小，以致吸附初期吸附質較難於吸附，而隨吸附過程的進行，吸附出現自加速現象，吸附層數也不受限制。

IV 型等溫線中間段出現吸附回滯環，其對應的是多孔吸附劑出現毛細凝聚的體系。在中等的相對壓力，為毛細凝聚的發生。中孔毛細凝聚填滿後，若吸附劑還有大孔徑的孔或者吸附質分子相互作用強，可能繼續吸附形成多分子層，吸附等溫線繼續上升。但在大多數情況下毛細凝聚結束後，出現一吸附終止平台，並不發生進一步的多分子層吸附。

V 型等溫線達到飽和蒸汽壓時吸附層數有限，吸附量趨於一極限值。同時由於毛細凝聚地發生，在中等的相對壓力等溫線上升較快，並有回滯環。

VI 型等溫線是一種特殊類型的等溫線，反映的是無孔均勻固體表面多層吸附的結果（如潔淨的金屬或石墨表面）。實際固體表面大都是不均勻的[11, 12]。

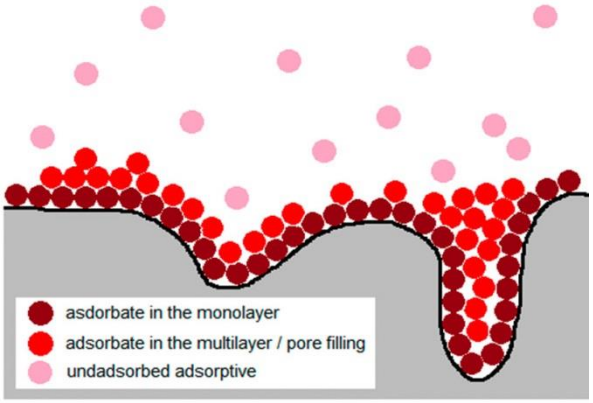

圖 2-4、單層吸附示意圖

圖 2-5、BET 測量儀器

功能說明	利用氣體吸附法量測材料之比表面積和孔徑分析
儀器服務項目	1. 比表面積分析。 2. 中孔、微孔孔徑分布分析。
樣品準備	比表面積小的樣品(< 100 m^2/g)，樣品重量約需0.3 g。 比表面積大的樣品(> 1000 m^2/g)，樣品重量約需0.1 g。

表 2-1、BET 儀器使用注意事項

第三章 實驗方法與流程

3.1 實驗流程

本研究以化學浴法，在不鏽鋼基板上沉積四氧化三鈷薄膜。再對四氧化三鈷薄膜進行分析。

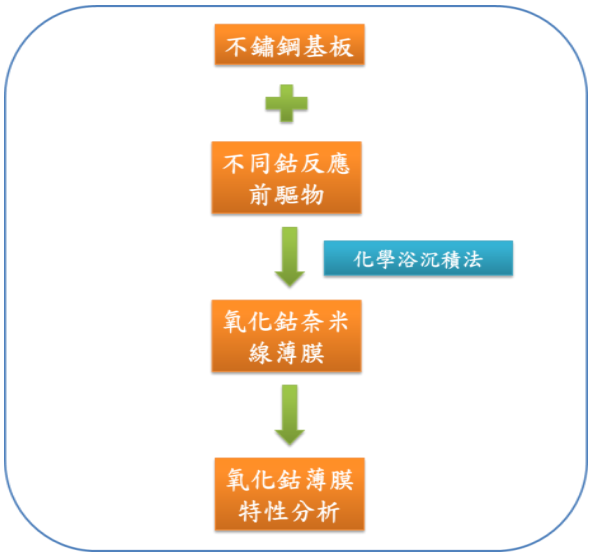

圖 3-1 實驗流程

3-2 實驗藥品

藥品名稱	英文名稱	分子式	純度	廠商
尿素	Urea	NH_2CONH_2	99.5%	Sigma Aldrich
硝酸鈷	Cobalt(III) nitrate hexahydrate	$Co(NO_3)_2 \cdot 6H_2O$	99.999%	Sigma Aldrich
氫氧化鉀	Potassium hydroxide	KOH	90%	Sigma Aldrich

3-3 多孔奈米線薄膜製作

3-3-1 基板前處理

(1). 基板浸入氫氧化鉀水溶液，置入超音波震盪機中去除油脂

(2). 基板浸入去離子水、酒精，置入超音波震盪機中反覆清兩次

(3). 基板置於加熱板上烤乾

3-3-2 四氧化三鈷薄膜製作

(1). 將 0.1M 硝酸鈷和 0.2M 尿素於去離子水中混合。

(2). 將清潔過的不鏽鋼基板浸入反應浴中，在加熱板上以 363K 下持溫 3 小時。

(3). 將試片取出，用去離子水清洗後置於加熱板上乾燥，接著 623K 下退火。

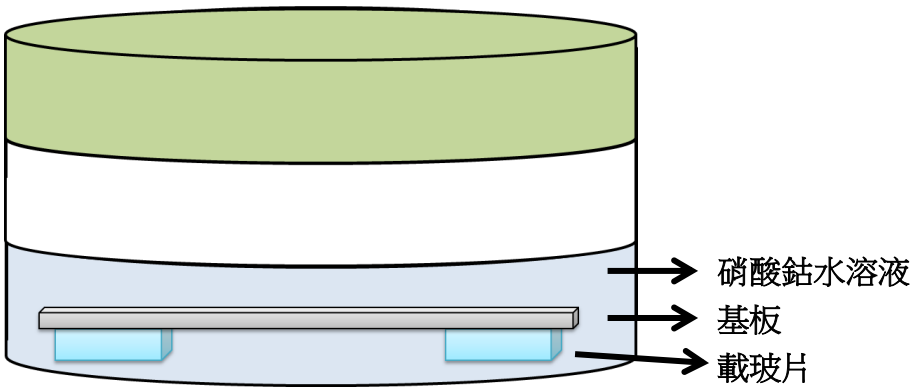

圖 3-2 化學浴沉積法示意圖

第四章 結果與討論

本實驗由化學浴沉積法在不鏽鋼積板上成長氧化鈷薄膜。本章將分為四個部分，第一個部分為奈米線結構氧化鈷薄膜的結構特徵分析，第二個部分為奈米線氧化鈷薄膜的表面特徵分析，第三個部分為奈米線氧化鈷薄的電化學特性分析，第四個部分為結論。

4.1 氧化鈷薄膜結構特徵分析

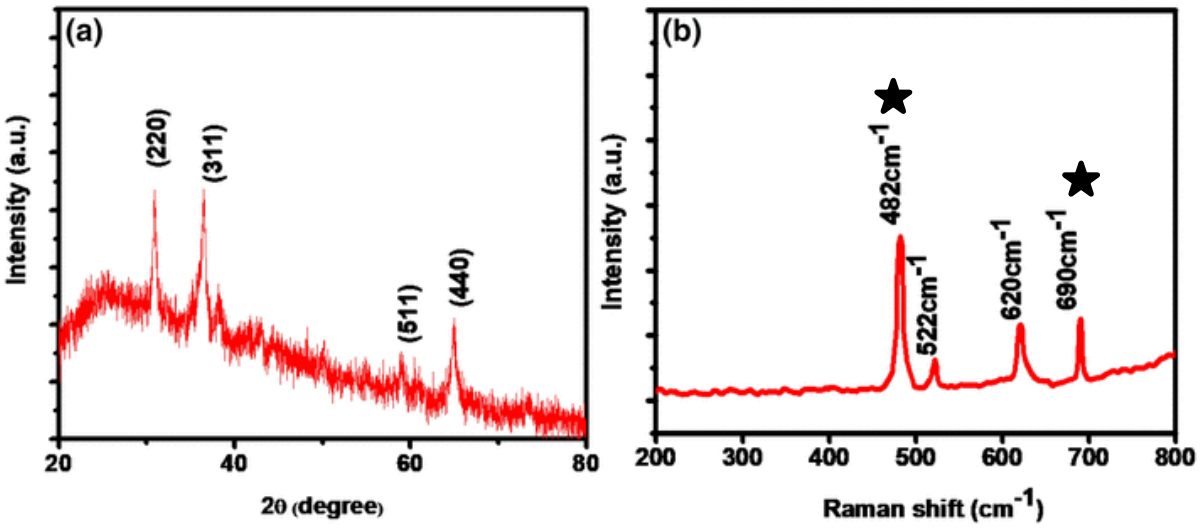

圖一、Co_3O_4的 (a) XRD 圖 (b) 拉曼光譜

圖一(a)為典型的氧化鈷 XRD 圖，為多晶立方結構的氧化鈷。平面(220)為主要的反射峰值，且與平面(311)和(511)相對應的其他峰值明顯較低，顯示出了高純度的四氧化三鈷。這些平面也與氧化鈷的標準 JCPDS 數據(卡號：78-1969)一致。且由於多個峰值，峰值間距並非等間距，可初步判定為多晶結構。

由圖一(b)拉曼圖中 482 cm^{-1}、690 cm^{-1} 的峰值確認為四氧化三鈷的氧化鈷型態。

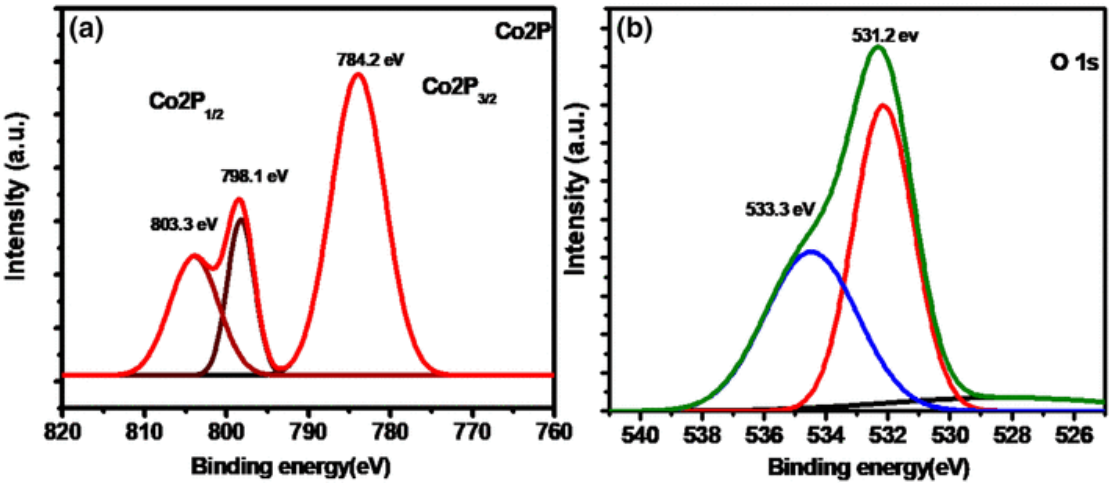

圖二、Co_3O_4的 XPS 圖

由圖二(a)可知 784.2eV 的峰值屬於 $Co2P_{3/2}$，代表了 Co^{2+}的存在，而 798.1 和 803.3eV 的兩個弱峰屬於 $Co2P_{1/2}$，代表了 Co^{3+}，更證實了氧化鈷型態為 Co_3O_4。圖二(b)中可知 531.2eV 的峰值為中心峰，是因為氧在 Co_3O_4 中的型態造成。(氧可能為 O^-、O^{2-}、O_2^-)。

4.2 氧化鈷薄膜表面特徵分析

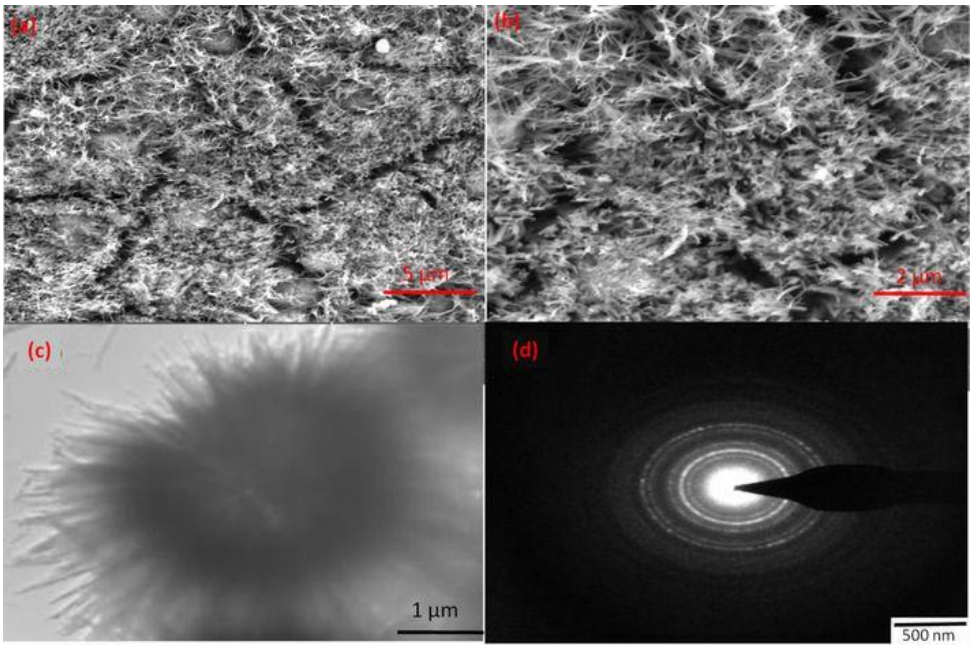

圖三、(a)5KX(b)10KX 的 SEM 圖、氧化鈷的(c)TEM 圖(d)SAED 圖

由圖三(a)和(b)知道氧化鈷薄膜為線狀氧化鈷形成的多孔薄膜。由(c)可確定此薄膜為氧化鈷晶體團聚而成。(b)中圍繞射環，代表了氧化鈷晶體為多晶結構，與 XRD 結果相同。

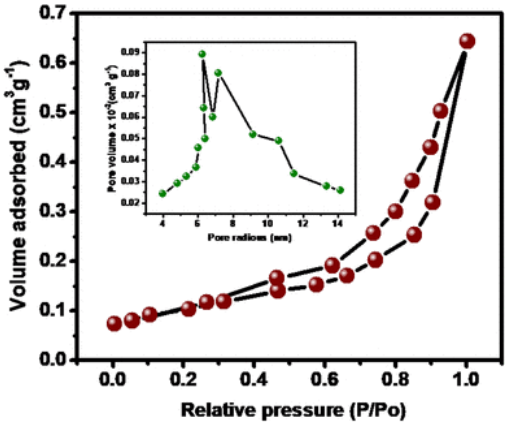

圖四、Co_3O_4的氮吸附脫附圖

圖四為氧化鈷的 BET 測量。圖中等溫線為 IV 型等溫線。氧化鈷的孔徑分布範圍為 4 到 14 nm**(參考文獻中誤植為 1 到 10 nm)**，平均半徑 1.43 nm，表面積為 66.33 m^2g^{-1}。超級電容器的能量密度主要取決於孔徑分佈和比表面積，本研究結果顯示了氧化鈷薄膜的高表面積有利於電荷儲存和大的孔徑使電解質離子和電子可有效傳輸分佈範圍，表 4-1 為與其他研究結果比較[13, 14]。**(原文獻中 Meher 的研究出處錯誤)**

	氧化鈷型態	表面積
本研究	奈米線薄膜	66.33 m^2g^{-1}
Meher	奈米片	60 m^2g^{-1}
Xiong	介孔	25.12 m^2g^{-1}

表 4-1

4.3 氧化鈷薄膜的電化學特性分析

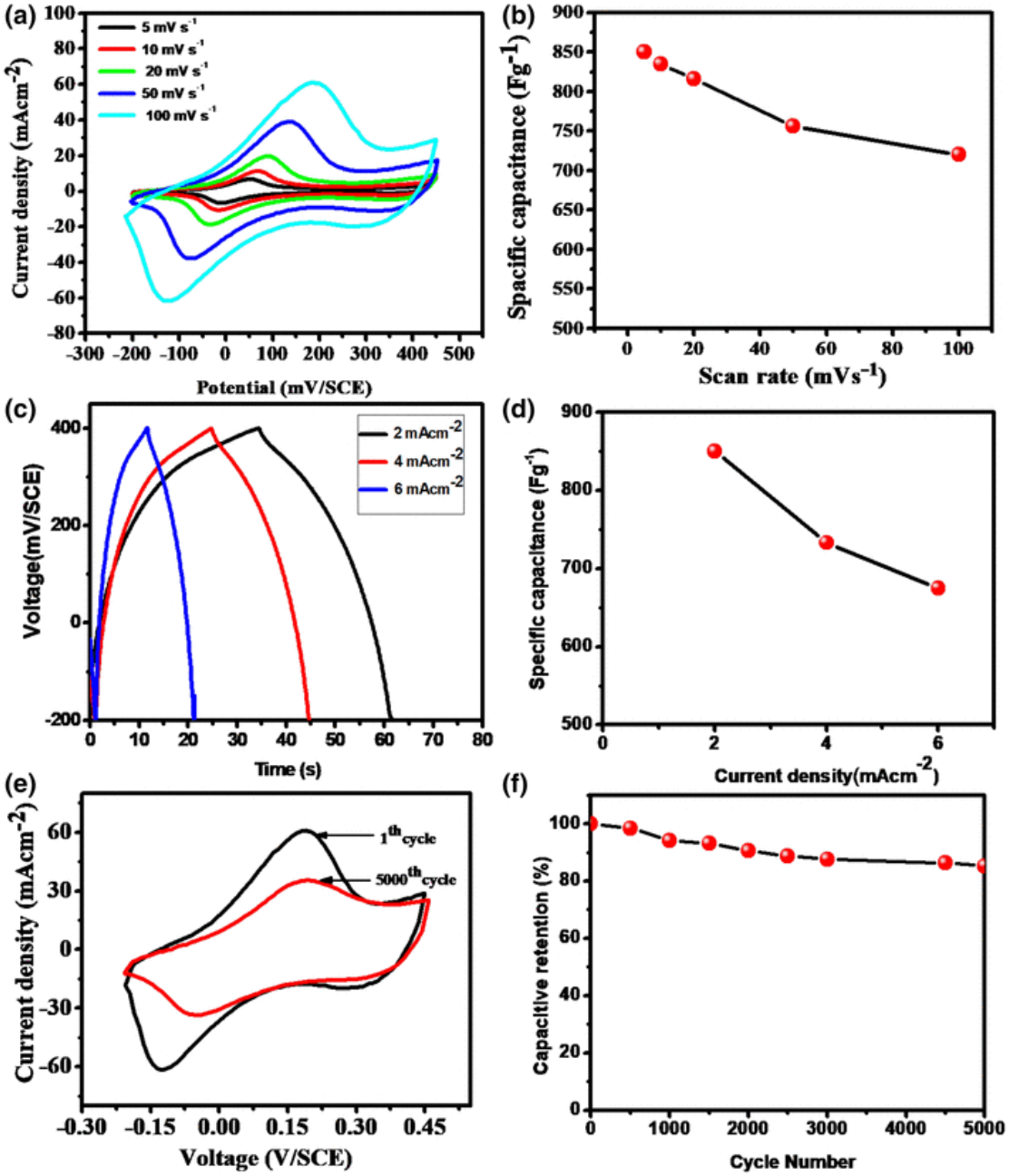

圖五、(a)不同掃描速率下的 CV 曲線、(b)不同掃描速率的 CV 值、(c)不同電流密度下的 GCD 曲線、(d)特定電流密度下的 CV 值變化、(e)掃描速率 100mV 下的電容穩定性、(f)不同循環數下的電容保留率

圖五(a)代表掃描速率為 5 到 100 mV^{-1} 時，在-0.2 到 0.45V 的電位窗中的氧化鈷

CV 測量圖，圖中具有氧化還原峰，代表氧化鈷具有擬電容特性，且 CV 曲線面積隨掃描速率增加而增加。圖五(b)中可知掃描速率 5 mV^{-1} 時具有最大的比電容值 850 Fg^{-1}，且比電容值隨著掃描速率增加而下降，這是因為電荷轉移不充分且電解質在此活性電極材料擴散有限，無法滿足較高掃描速率下的電化學反應。圖五(c)中的 GCD 曲線偏離直線，代表氧化鈷具有擬電容特性，與(a)顯示的結果相同。圖(d)中在電流密度 2 $mAcm^{-2}$ 時有最大的比電容值 825 Fg^{-1}，隨著電流密度增加，比電容值下降，因為在高電流密度下僅有電極表面活性物質發生氧化還原反應。圖(e)為掃描速率 100 mV^{-1} 下的 5000 次 CV 循環，是為了測定氧化鈷用於超級電容的穩定循環，而選用掃描速率 100 mV^{-1} 是因為其 C 曲線圖的面積較大，較易觀察圖形變化。由圖可看出第 5000 次的 CV 圖仍保有氧化還原峰，代表了氧化鈷的優異循環穩定性。圖(f)顯示出在 5000 次循環時仍有 86%的電容保留率。

4.4 結論

本研究之奈米氧化鈷於超級電容器之應用具有相對優勢，以下分兩點論述之：

一、奈米線結構在超級電容器上更具優勢。此結構在電化學反應時與電解質液更有效接觸和有利於電子傳輸、高比表面積有利於電荷儲存、適當孔洞可供電解質液和電子的傳輸。

二、基板的選擇使氧化鈷於應用上更具優勢。直接生長在不鏽鋼基板上的氧化鈷奈米線薄膜避免了黏合劑或添加劑造成的界面和缺陷[13]、生長不均勻、以發泡鎳為基板而再現性差的情形。

針對本研究，筆者相關建議如下：

一、研究者應說明使用的不鏽鋼基板為何？是不鏽鋼編織網或是其他，若為不鏽鋼編織網，其孔徑大小和孔目數量。如此才能使後人如同站在巨人的肩膀上，使奈米氧化鈷應用於超級電容之研究更進一步。

二、研究者應說明本研究中 BET 測量結果中 IV 曲線代表特性與奈米線氧化鈷薄膜之超級電容特性間的關係。

三、比電容保留率應該要用具有最大比電容值的掃描速率 5 mV^{-1} 而不是 100 mV^{-1}。且亦應說明比電容保留率為何僅 86%？因為 Xiong 的片狀氧化鈷雖然比電容值較低，但由於其結構穩定，因此電容保留率達 93%[15]，故 86%的電容保留率是奈米線氧化鈷薄膜結構不穩定、體積膨脹或其他因素造成，研究者應當更深入探討之。

第五章 口頭報告簡報

5.1 簡報圖檔

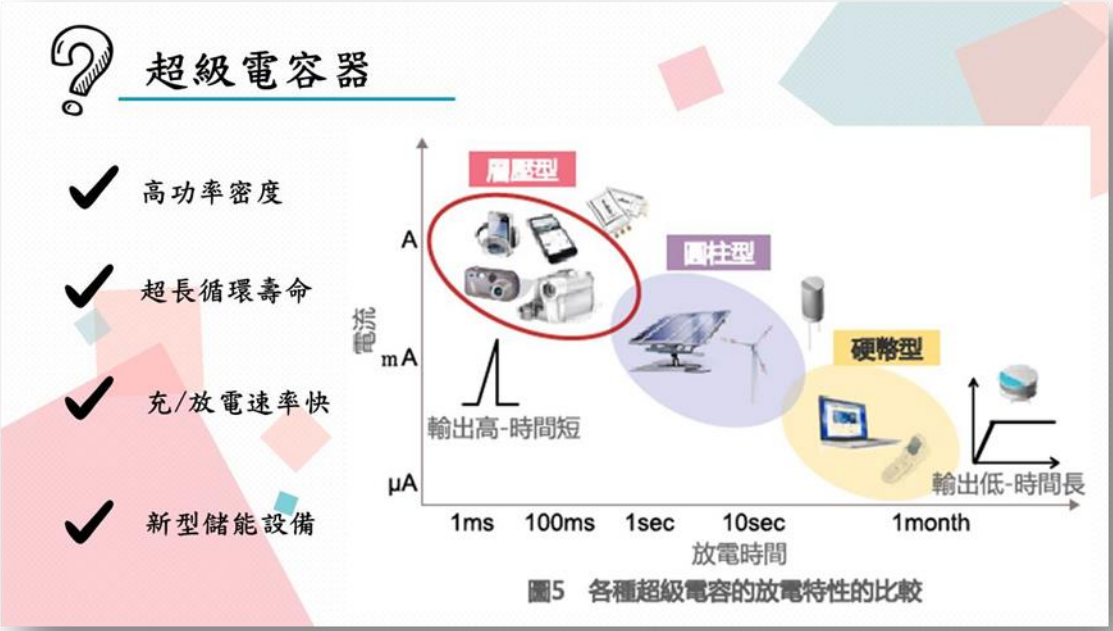

圖5 各種超級電容的放電特性的比較

超級電容器與傳統電池比較

	超級電容器	傳統電池
充電時間	毫秒至秒	1-10小時
能量密度	1-5 Wh/kg	8-600 Wh/kg
循環壽命	>10萬個週期	150-1500個週期

超級電容器分類

	對稱型	非對稱型
電極材料	相同	不同
特性	電壓值受限大	電壓值易提升

超級電容器分類

	電雙層電容	擬電容
儲能機制	電荷分離	氧化還原反應
電極材料	碳	金屬氧化物
比電容值	250 Fg^{-1}	700 Fg^{-1}

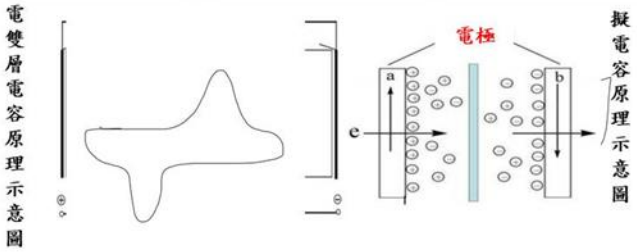

Co_3O_4奈米線結構

- ✔ 環境友好性
- ✔ 高理論電容(3560 Fg^{-1})
- ✔ 高表面積與體積比

化學浴沉積法
(Chemical Bath Deposition, CBD)

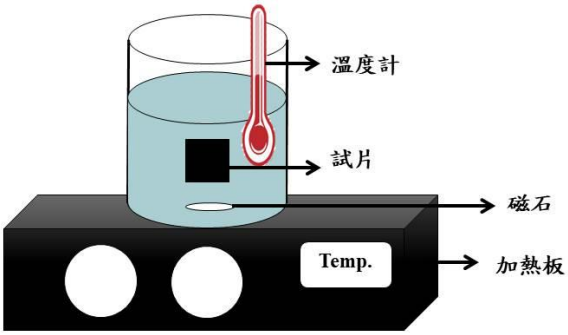

- ✔ 成本低
- ✔ 適合大面積表面薄膜生長
- ✔ 生產CIGS或CdTe薄膜太陽能電池的重要步驟

比表面積與孔隙度分析
BET(Brunauer-Emmett-Teller)

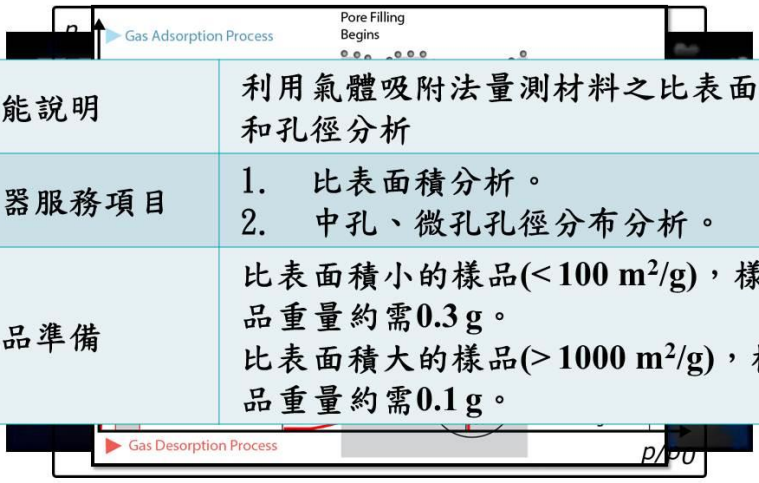

功能說明	利用氣體吸附法量測材料之比表面積和孔徑分析
儀器服務項目	1. 比表面積分析。 2. 中孔、微孔孔徑分布分析。
樣品準備	比表面積小的樣品(< 100 m^2/g)，樣品重量約需0.3 g。 比表面積大的樣品(> 1000 m^2/g)，樣品重量約需0.1 g。


PART
2
實驗步驟

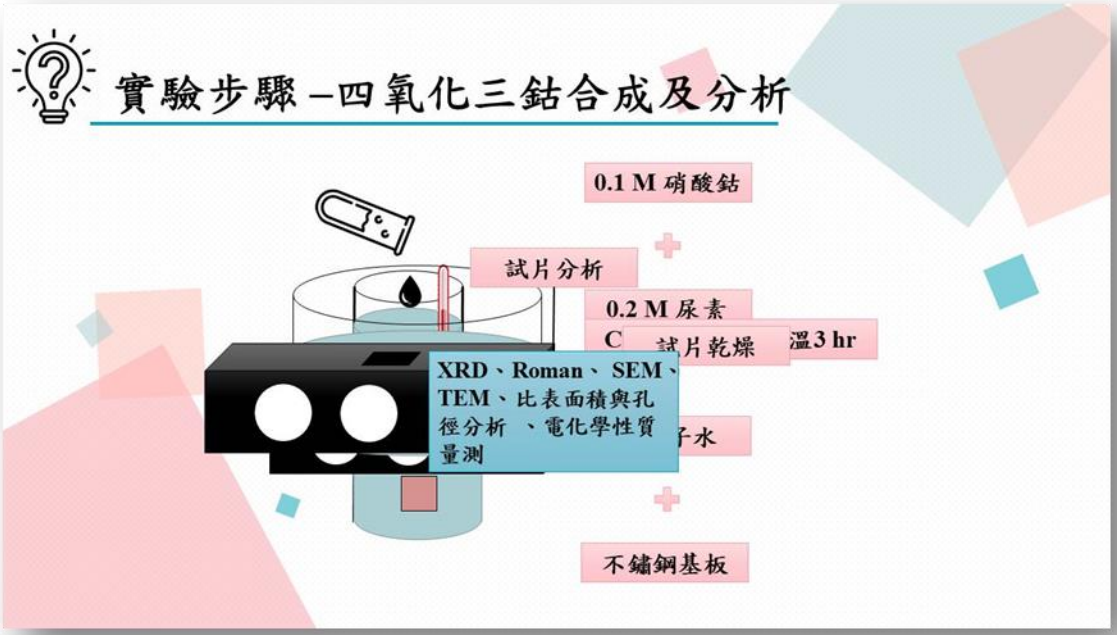
實驗步驟－四氧化三鈷合成及分析
0.1 M 硝酸鈷
試片分析
0.2 M 尿素
試片乾燥
溫3 hr
XRD、Roman、 SEM、TEM、比表面積與孔徑分析 、電化學性質量測
不鏽鋼基板


PART
3
實驗結果
與討論

氧化鈷薄膜結構特徵分析

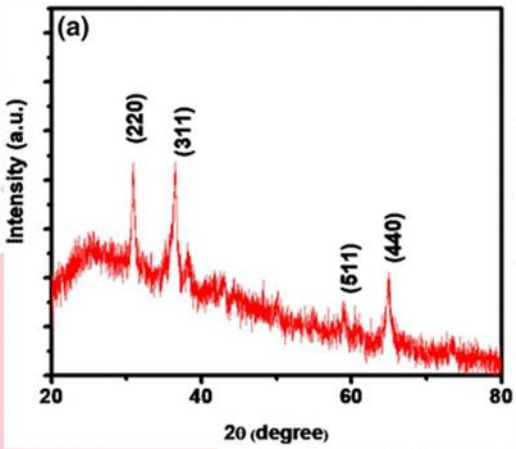

- 圖(a)為典型的氧化鈷XRD圖，平面(220)為主要的反射峰值，且與平面(311)和(511)相對應的其他峰值明顯較低，顯示出了高純度的四氧化三鈷。
- 平面也與氧化鈷的標準JCPDS數據(卡號：78-1969)一致。
- 多個峰值，峰值間距並非等間距，可初步判定為多晶結構。

氧化鈷薄膜結構特徵分析

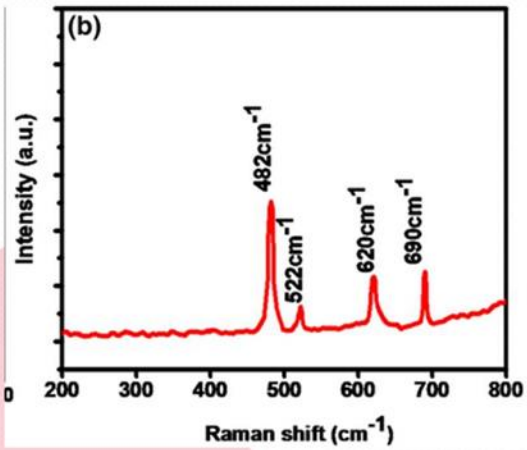

圖(b)拉曼圖中482 cm^{-1}、690 cm^{-1}的峰值確認為四氧化三鈷的氧化鈷型態。

氧化鈷薄膜結構特徵分析

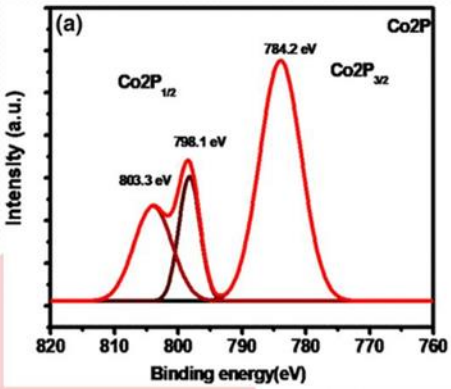

- 圖(a)XPS中784.2eV的峰值屬於$Co2P_{3/2}$，代表了Co^{2+}的存在
- 798.1和803.3eV的兩個弱峰屬於$Co2P_{1/2}$，代表了Co^{3+}
- 更證實了氧化鈷型態為Co_3O_4。

氧化鈷薄膜結構特徵分析

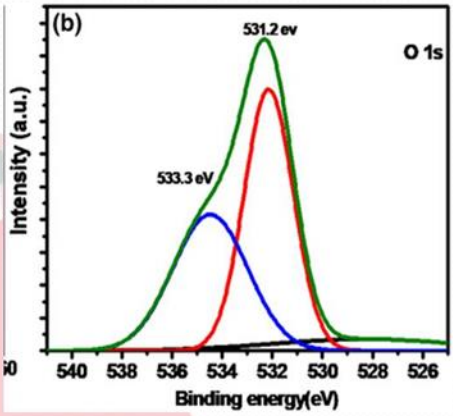

圖(b)XPS中可知531.2eV的峰值為中心峰，是因為氧在Co_3O_4中的型態造成。(氧可能為O^-、O^{2-}、O_2^-)。

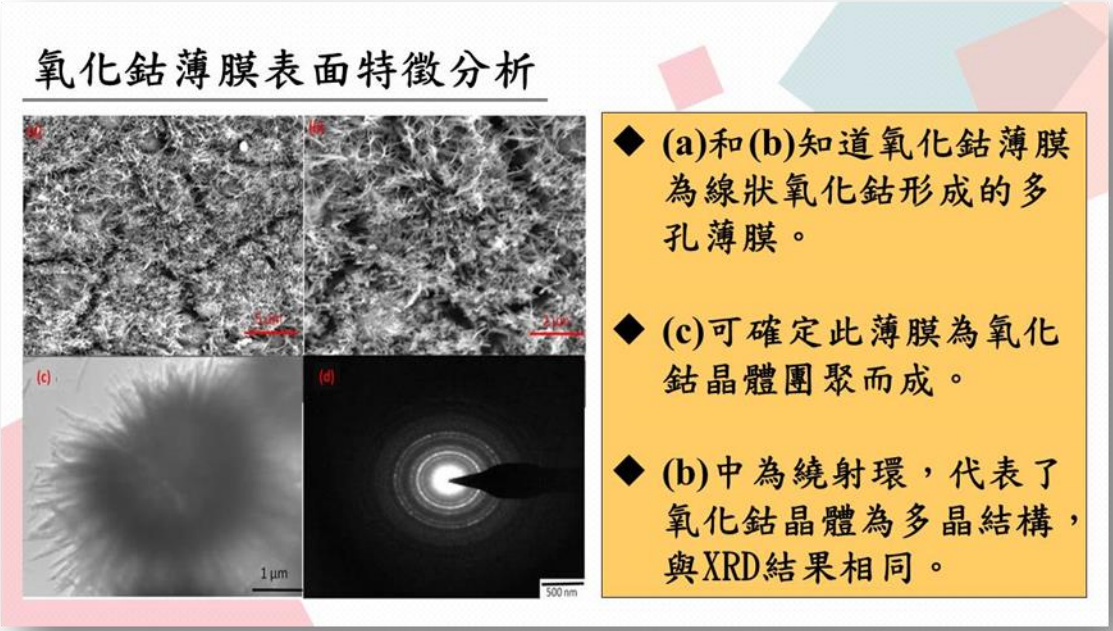
氧化鈷薄膜表面特徵分析
(a)
(b)
(c)
(d)
1 μm
500 nm
◆ (a)和(b)知道氧化鈷薄膜為線狀氧化鈷形成的多孔薄膜。
◆ (c)可確定此薄膜為氧化鈷晶體團聚而成。
◆ (b)中為繞射環，代表了氧化鈷晶體為多晶結構，與XRD結果相同。


氧化鈷薄膜表面特徵分析
圖為氧化鈷的BET測量。
◆ IV型等溫線
布範圍
獃中誤
Volume adsorbed (cm³g⁻¹)
Relative pressure (P/Po)
0.0
0.1
0.2
0.3
0.4
0.5
0.6
0.7
原理説明
ガス吸着量
相対圧力
movavi
表面積
6.33 m²g⁻¹
60 m²g⁻¹
Xiong
介孔
25.12 m²g⁻¹

氧化鈷薄膜的電化學特性分析

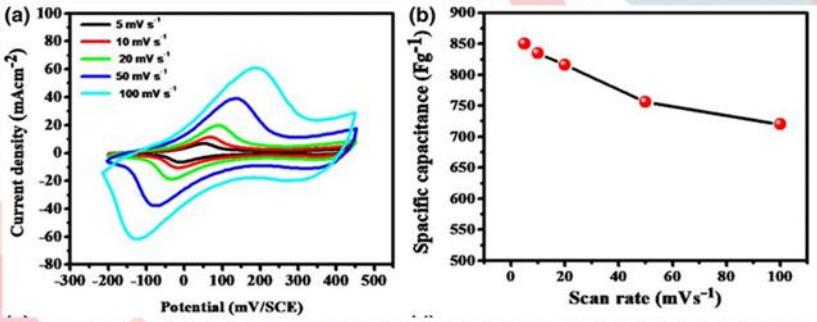

◆ (a)代表掃描速率為5到100 mV^{-1}時，在-0.2到0.45V的電位窗中的氧化鈷CV測量圖，且CV曲線面積隨掃描速率增加而增加。

◆ (b)中可知掃描速率5 mV^{-1}時具有最大的比電容值850 Fg^{-1}，比電容值隨著掃描速率增加而下降

氧化鈷薄膜的電化學特性分析

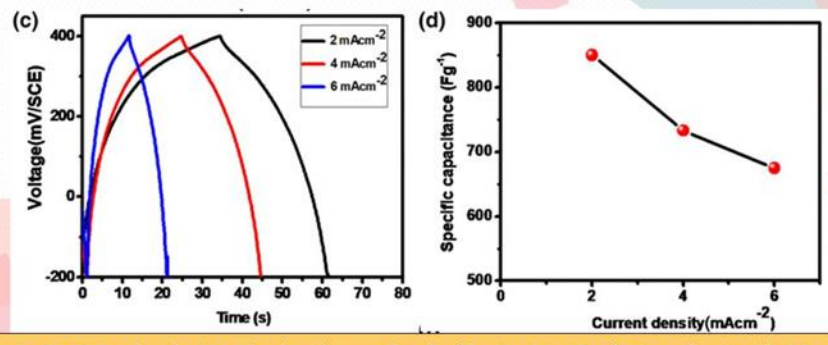

◆ (c)中的GCD曲線偏離直線，代表氧化鈷具有擬電容特性。

◆ (d)中在電流密度2 $mAcm^{-2}$時有最大的比電容值825 Fg^{-1}，隨著電流密度增加，比電容值下降

氧化鈷薄膜的電化學特性分析

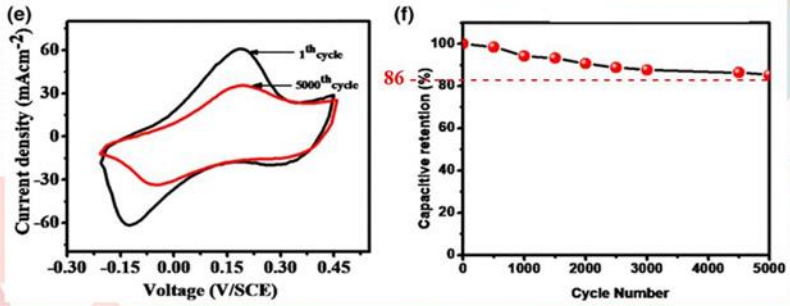

◆ (e)為掃描速率100 mV^{-1}下的5000次CV循環，是為了測定氧化鈷用於超級電容的穩定循環。

◆ (f)顯示出在5000次循環時仍有86%的電容保留率。

結論

- 氧化鈷奈米線的結構非常適合在電化學反應時與電解質液有效接觸和電子傳輸。
- 在不鏽鋼基板上生長可避免生長不均勻或以發泡鎳為基板的而再現性差的情形，更適合作為實際應用。

[1] A. A. Yadav, Y. M. Hunge, and S. B. Kulkarni, "Chemical synthesis of Co3O4 nanowires for symmetric supercapacitor device," *Journal of Materials Science: Materials in Electronics,* vol. 29, pp. 16401-16409, 2018/10/01 2018.

[2] https://www.murata.com/zh-cn/products/emiconfun-tw/capacitor/2015/03/24/tw-20150324-p1。

[3]連婕。「鎳系-石墨烯/植物纖維於可撓式非對稱性超電容器之研究與應用」。碩士論文，國立中興大學化學工程學系所，2014。

[4] http://www.enedu.org.tw/technology/tech-3.php

[5] http://140.114.47.150/Researchfields03.html

[6] https://www.manz.com/tw/technologies/wet-chemistry/coating-plating/

[7]林逸傑。「化學浴沉積法製備孔洞性四氧化三鈷奈米片薄膜應用於一氧化碳氣體感測之特性研究」。碩士論文，國立交通大學材料科學與工程學系所，2014。https://hdl.handle.net/11296/nvvd36。

[8]http://ir.lib.ksu.edu.tw/bitstream/987654321/21207/2/%E5%B0%88%E9%A1%8C%E8%A3%BD%E4%BD%9C.pdf

5.2 口頭報告參考資料

[1] A. A. Yadav, Y. M. Hunge, and S. B. Kulkarni, "Chemical synthesis of Co3O4

用於對稱超級電容器之氧化鈷奈米線化學合成

nanowires for symmetric supercapacitor device," *Journal of Materials Science: Materials in Electronics*, vol. 29, pp. 16401-16409, 2018/10/01 2018.

[2] https://www.murata.com/zh-cn/products/emiconfun-tw/capacitor/2015/03/24/tw-20150324-p1。

[3]連婕。「鎳系-石墨烯/植物纖維於可撓式非對稱性超電容器之研究與應用」。碩士論文，國立中興大學化學工程學系所，2014。

[4] http://www.enedu.org.tw/technology/tech-3.php

[5] http://140.114.47.150/Researchfields03.html

[6] 亞智科技塗布與電鍍技術介紹

https://www.manz.com/tw/technologies/wet-chemistry/coating-plating/

[7]林逸傑。「化學浴沉積法製備孔洞性四氧化三鈷奈米片薄膜應用於一氧化碳氣體感測之特性研究」。碩士論文，國立交通大學材料科學與工程學系所，2014。https://hdl.handle.net/11296/nvvd36。

[8]http://ir.lib.ksu.edu.tw/bitstream/987654321/21207/2/%E5%B0%88%E9%A1%8C%E8%A3%BD%E4%BD%9C.pdf

第六章 「專題討論」筆記與 Q&A 問答集

6.1Q&A 問答集

用於對稱超級電容器之氧化鈷奈米線化學合成

Q1.使用發泡鎳作為基板與不鏽鋼作為基板的差別？

A1.發泡鎳為隨機發泡，做為要實際應用的超級電容器，對於產品的穩定性和氧化鈷的再現性有所影響。但不鏽鋼基板的每一批的表面形貌是相同的，因此以不鏽鋼作為基板的奈米線氧化鈷薄膜的再現性和產品穩定率相對較好。

Q2.BET 量測為何使用氮氣？

A2.氮氣為表面惰性氣體，且形狀接近球體，可更好的模擬電子儲存的型態。雖然氦氣和氖氣同為惰性氣體，但相對來說，純氮氣更容易取得，價格較便宜。

6.2 課堂筆記

藍色字體為同學報告時的內容筆記，紅字為提問的問題，綠字為老師課堂補充的內容，**黑字**為自己上網查詢的資料而非同學報告內容。

3/8 ① 梁：老鼠皮下植入鈦、鎳、鈮，玻璃性支架

靜態培養：硼酸鹽玻璃有毒
訂 〃 〃 〃 〃 無〃 > Q：這啥？為什麼要硼酸鹽？

✓Q 支架皆具多孔結構 Q 用意？

✓Q：為何用鈦、鎳、鈮？

② 威：3D - 氧化鈷用於石墨烯

母石墨烯為3D發泡結構，by ~~CVD 沈積~~ Co_3O_4 水熱.
↳ 高比表面積

✓Q 發泡是本來的？再現性？如何確保溶液滲入孔狀結構

Q 為何氧化鈷可藉此降低电阻，提升电荷移転.？

✓Q 發泡鎳 + 乙醇 → 3D 石墨烯

✓Q 奈米线生长密集，是否会影响？

③ 溫：石墨塗食对引擎磨耗之研究

活塞运动磨耗造成吃机油.

石墨 → 固体潤滑劑 → 減少磨耗

硬塗层：耐磨、高硬度（优）；損坏氣缸壁（缺）
軟 〃 〃：高溫產生毒性（先用 MoS_2）、側压力

石墨塗层之磨損為磨粒磨損.

老師講評：秀一下 paper 沒特別解釋的 ex. CVD、球磨、水熱.
↳ hydrothermal synthesis

要延伸解釋自己要講的東西.（by 图片 etc.）

■：老師講解

3/15 ② 古：靜电紡絲 → 溶液射出帶电荷，因有黏度呈絲狀.

PVDF：空気过濾 + NGP：电荷儲存. → 纖維膜过濾空気 99.9%.

物理屏障 + 黏彈性 → 駐極体：本身帶靜电，帶电粒子經过被吸附

✓Q 靜电紡絲？ ✓Q. 1 坪、2 坪都 98%

③ 詹：气流濺鍍熱塑阻障层（TBC）→ 用於燃燒室.

用於：飛机引擎，渦輪發电机.

真空陰極鍍膜（气流濺鍍）：氧化鋯已穩定的氧化鋯，对狀結構給体積膨脹的空間.
↗ 氧化鋯中加入氧化鈣，其以 Mg、Ca 也有同样效果
↓ 相穩定 → 使氧化鋯不於高溫時体積膨脹 1~2%

650°C、900°C、800°C ✓ 最高. ✓Q 超过 800°C？

P.1

3/25 ④ 煒：TiO_2中 ALD 沉積 nano 用於光催化生成 H_2.
原子层沉積.
不同尺寸之奈米管長对比有不同適合參數.
*解釋的部分往前放.

4/15 ① 飞：MoS_2 @ Co_3O_4
↓
低電子特性，低能耗，高儲能.
6 方結構.(MoS_2)
2 个氧化还原峰；循环稳定 87%.

Q.✓ *氧化还原图.
1个氧化还原峰 → 2次电荷转移.

② 樣：TiO_2 納米管，光催化降解百草枯（除草劑）
✓Q. 碳化？ p.3.
TiO_2 僅在紫外光区具活性，且表面積小，用奈米管構造.

③ 的奈粒子 3 色振測 → 3 峰波长 → 農藥，具半衰期，殘留於水、食物.
原理. 簡单，便宜.

④ 晉：X

⑤ 育：X

前部分解釋清楚，結論可以不用細說，个子 paper 給的啟發.
搞清楚題目之中心思想.

4/20 ① X

② 邱：奈米纖維製造 by 靜电紡絲.
↳ 高比表面積、直徑小.

p.15 距離先討論最小距離，討論最去效應.

③ 彦：TiO_2 / ZnO / Pt 複合电極增強甲醇氧化电催化活性.
直接甲醇燃料电池：質子交換膜电池，应用：手机、notebook、发电机.
↳ 发电效率低，甲醇穿透，反应物处理
FTO + TiO_2 + ZnO + Pt ✓Q. Why 这样的順序，選材原因？
CV CV. 主要催化 ∴ 最後.
Ti、Zn 半導体性質，Pt 高活性.

④ 翔：Co_3O_4 @ $NiCo_2O_4$ 超級电容.
✓ 選擇发泡鎳的原因，常規聚集和高能量打散，why 可以？
解決

高分子溶液
✓Q. 金属溶液可噴？
目前多為高分子（密度 1~2）陶瓷（密度 2~3）。金属（密度：~10），太重無法射出成型，溶液內的量必須非常少.

P.2.

⑤ 信 X

⑥ 深：CdS @ CeO_2 可見光下光催化还原 CO_2.

CdS：窄能隙 / 較不穩定（光腐蝕），再結合辛吉

CeO_2：無毒，穩定 / 寬能隙

Q. 有毒.

Q. 稀土元素.

CdS → CeO_2.

4/22 ① 條：X

② 盈：片狀石墨鑄鉄的石墨結構和等軸.

非破坏檢測磁等軸.

磁自適应式檢測磁量，研究鑄鉄性能，最敏感手法之一. (MAT)

Q why?

③ 李：銅奈米粒对大腸桿菌的抗菌行為

銅能发挥卓越殺菌效果：攻擊，抑制細菌，对抗真菌效果佳

Q 銅如何做到？破坏了細胞膜，造成凹坑.（抗菌机制：銅離子对細菌細胞的强烈吸附）

UV-Vis 分光光度計：菌苔增加，溶液变混濁.

Q 实際应用？医院耗材、濾網、繃帶.

③ 潘：銅鎢氧化物，二氧化鈦（p型半導体）CO 氣体感測器.（半導体式）→ Q 與其他方式之比較？不知.

n型半導体

↳ 氣体吸附作用.

200 ppm 時不適，1600 ppm 死亡.

p-n 可增加氣体感測器的效能.

測量時改變速度 選擇性

speed selectivity

S

stability 反應多次後的穩定度 低含量時不会团聚

sensitivity 敏感度

④ 豐：氧化石墨烯降解……

生物可降解高分子 → CO_2、水.

用於PLA、PBS

Q why 要在真空烘箱中烘烤？

60 不会影响 PBS 的晶体結構.

儲能模数 ⇒ 看加機性能

感測器於物联網很重要. (IDT)

補 4/15 ④：晉：奈米材料用於水解氫

能帶越窄，电子-电洞对再結合机率低 ⇒ 產氫效率收.

Q 氫能应用上的最大瓶頸？ 儲氫

生物產氫的成本並不高，生產綫可大，但"氫"並不純，需額外其他物質分離

(机油、廚餘被細菌吃 → 產氫)

P.3.

5/29 ① 鐘：1ML 吡啶氯，0.1ML 苯氯 超級电容

Q 这什么？雜环碳

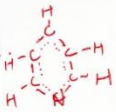

鹼性葉 → 摻雜氮的活性碳.

NKGLC → 擬电容.

② 柯：电漿滲碳法

DLC 薄膜：高硬度，固体潤滑剂，耐磨，耐蝕 → 可用於飛机发动机.

類鑽石(450°C) sp^3 + sp^2 結構，顏色：黑色. 1000°C↑

Q 3种滲碳的优缺点？

固滲：优點 簡单

氣滲：緻密

电滲：最緻密，時间最高.

③ 黃：鈷摻雜氧化鋅薄膜 → 甲醛感測器.

from 藍宝石基底 Q why 不用一般的 Al.

單晶、導熱佳

④ 蔣：MnO_2 沉積在奈米碳管.

Q 哪一种超級电容：氧化还原的 ∴ 互混合型

MnO_2：成本低，理論比电容佳 but 導电率差.

科技的发展未直於一直问问題！

Q 4.3 的演講会先丟一個問題後，再自己回答，目的：抓住觀眾，讓他們思考.

超級电容 v.s. 电容：充放电速率不同.

自己的報告 後檢討：語速放慢！9分21秒！指標按彩筆怎用

CNTs → 奈米碳管.

↳ 表複數

ppt 修改部分

SEM 倍率 x5000 改 → 5KX.

BET：抽干材料內氣体 → 充入 $N_2(g)$ → 透过压力变化. → 反推比表面積 (m^2/g)，放 BET 原理圖 (Google 搜：BET theory)

離論可放心智圖.

P.4

5/6 ① 博：含可生物降解高分子和離子液体的綠色混合物

本篇用：PHB → 能量儲存物質，質地硬脆.

[EPRI][TFSI]
↳ 含此的液体直接熱穩定性

DSC 熱分析 → 離子液体↑，Tg↓，∴ 釋出了 PHB.

② 勝：porous carbon @ MnO_2.

~~N-doped PC + PC @ MnO_2~~ PC @ MnO_2 // NPC

Mn 3s 峰決定 Mn 的氧化物形态.

VQ P.15 (b)  IR drop ∴ 要跨过电位压，而損失的能量以熱能散失

③ 宗：印刷印製備摻鍶的介孔生物活性玻璃 — 用於骨再生

離子濃度的釋放会影响細胞.

④ 鼎：PCL + 新型離子液 混合的性質与非性質动力学.
↳ 低溶点離子化合物
↓
高分子有高的混溶性，可分解高分子. ∴ Tg = -60°C，Tm = 60°C

VQ DSC 分析原理. VQ. 性質 & 非性質动力学研究目的

④ 燕：熱 & 光影响鈦鈦矿的不稳定

VQ why 用 plasma 处理後旋塗的液体更容易附著？ < 清潔. 表面沉積親水端.

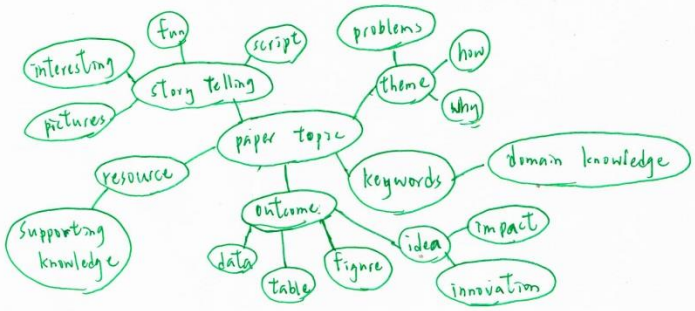

P.5

5/13 ① 惟：奈米碳 + 石墨烯不同比例下的超級电容器.

电池 + 电容器 = 超級电容器.

石墨烯：高導熱、电和大表面積.

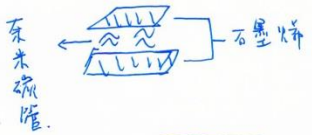

GS-CNTs - 9-1 觀察多且無互相堆疊
↓
可提升比表面積.

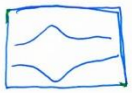

Q. 用在哪种超級电容器？

② 穎：~~融在~~ ~~溶劑~~ ~~膜~~. 奈米銀漿在於 PET 紙.

③ 郭：金奈米粒子比电流氣有和磷異樂戒測

奈米金有电漿共振 (SPR)、特殊电性和光性.

·用电沉析（緩蝕劑）作文測試.

Q 如何使金奈米"均勻分散"在溶劑？

A. 表面改質：① 电荷狀況 ② 形狀.

SERS.
奈米金有表面电場，打拉曼時能增強訊号.

塑料夾 / AuNP夾 / 棒吸收夾 / 塑料夾.
↓
Q. 這是什麼 & 目的？ 吸收多餘液体.

Q 用金什麼特性？
碰到異樂會变色 ∵ SPR.

④ 昱：奈米多孔多鈦矽為阳極的鋰电池.

石墨：缺：体積变化太大 → 电極結構粉碎（充电時）

Q. why.?

→ 用奈米多孔結構解決 — Why 可以解決？
+
PPAN 作為碳基电組織，適應体積膨脹.

Pratice makes perfect. Preparation makes pratice.

· 能量 (J) ≠ 功率 (W).

	电池	超級电容
	↓ chemi rxn	↓ 电.
∴ 能量密度	大	小
功率密度	小	大.

方式.

Faraday	(氧化还原)
H+T	
Helmholtz	(静电)

P. 6

5/20 ①：鎳：危害的活碳

C_{12}~C_{18} C_{20}~C_{40}

煤油，蠟燭活碳.

液氣，真空，離子，固體，氣体活碳法.

② 好：雷射圖案化聚酰亚胺酰亚胺用於推測醫支撑架

細胞無毒性，but 生物惰性 → 無法使細胞附著.

→ 用雷射蝕刻造的表面紋理.

Q. 遮罩是哪种遮罩？不解危害.

③ 林：X

④ 荊：釋放負離子 & 阻挡 PM2.5 的低阻抗过濾膜.

的效功效.

用静电紡絲.

材料對於絲的孔徑影响小.

高机械过濾效果，穩定电荷穩定性.

⑤ 梓：氧化石墨烯很難結晶且水解降解.

可分解高分子與低統塑膠有相似的物性.

GO 為他会降低水解能力；太高会阻礙高分子結晶.

Q. 机械性質可與一般不可分解高分子相比嗎？

• Laser：light amplifer of stimulated emission of radiation ← 量子力学 / 固态物理 / 电磁学.

- lasing media ← 固态 / 液态 / 气态.
- light

① 光波同調性 ② 能量集中

③ 不易散射.

AnF* → 不穩定 ∴ 激态回復时放光.（气体雷射）

染料雷可調整光的波长（液态雷射）

• 空气濾清：① 静电 ② HEPA

P.7

5/27：① 翌：X

② 時：X

③ 芸：鎳合金微弧氧化製備 → 耐磨.

MAO：製程中，電漿在高溫高壓，使結構產生變化

V_2O_3、MnO_2 使 MAO 塗層變黑色

VQ：黑色：美觀，

自己上網查到：黑色微弧氧化多陽極處理的一種。
此陶瓷層可耐於高溫，強光仍保有抗紫外線
之物性，不會褪色。除光學物性需求外，亦適
用於真空，航太…等熱傳導物件.

※一個好的演講，要給觀眾想學的理由.

演講要控制語調

眼神要與觀眾有接觸.

6/3：① 石：SnO_2 超級電容.

FCC 碳纖維為離子和電子提供通路.

SnO_2 包裹 FCC (Functionalized carbon cloth)

VQ：why 禮.數多，電容保留率低 → paper 沒寫.

② 炫：CVD 成長石墨烯作為酸性電解液的催化劑.

3D 石墨烯具高催化能力，↑電荷轉移快 & 高液/氣滲透性

3D 發泡鎳為基板使石墨烯成長. → 蝕刻掉發泡鎳，
銷酸.

→ PC 為基底放 3D 石墨烯

→ 清洗不純，再燒鹽酸 Pt.

→ 無法完全替代，但可以減少 Pt，單位面積 5% 用量

P.8

目的：可生物降解高分子之結晶和机械性能.

PLLA.
↳ 脆性、結晶速率緩慢.

PEA、PLLA 兩種不相容 → PEA 分佈在 PLLA 中.

PEA 会降低 PLLA 結晶速率，有延遲情形.

会提升 PLLA 的韌性

√Q 表面变粗糙，韌性得到改善 → 細絲狀.
斷裂面.

補報告：5/27 的黃豐：活性氮化碳用於超級电容.
ACN

雜原子 (B、N、P、S) 輸入碳基質產生擬电容特性，提高电子和離子扩散，→ 比电容值提升.

KOH 活化後的大表面積和氧化面積.

* 林的演講的 20 C.

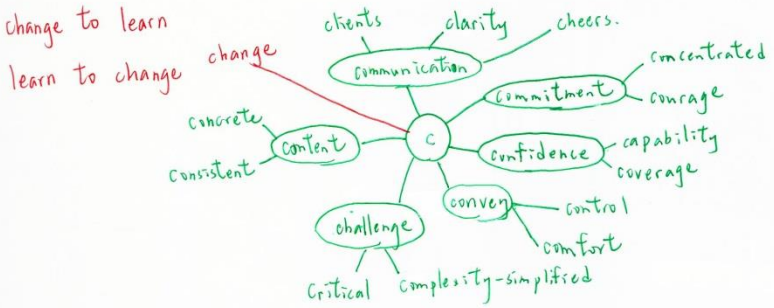

6.3 主要參考文獻

Journal of Materials Science: Materials in Electronics (2018) 29:16401–16409
https://doi.org/10.1007/s10854-018-9731-7

CrossMark

Chemical synthesis of Co_3O_4 nanowires for symmetric supercapacitor device

A. A. Yadav[1] · Y. M. Hunge[2] · S. B. Kulkarni[1]

Received: 11 May 2018 / Accepted: 23 July 2018 / Published online: 24 July 2018

Abstract

In present work, Co_3O_4 nanowire is successfully prepared on stainless steel substrate by simple chemical bath deposition method and studied the supercapacitor application. The prepared Co_3O_4 nanowire is analyzed by X-ray diffraction, X-ray photoelectron spectroscopy, field emission scanning electron microscopy and Brunauer–Emmett–Teller techniques. Co_3O_4 nanowire offers high specific surface area of 66.33 $m^2\ g^{-1}$ for the intercalation of electrolyte ions. Co_3O_4 nanowires exhibit outstanding electrochemical performance with a high specific capacitance of 850 F g^{-1} at scan rate of 5 mV s^{-1}, and excellent long-term cycling stability (86% over 5000 CV cycles). The symmetric solid-state supercapacitor device is fabricated by accumulating two electrodes of Co_3O_4 nanowire, which shows superior electrochemical performance with specific capacitance of 127 F g^{-1}, specific energy of 24.18 Wh kg^{-1} and excellent cycling stability (85% over 3000 CV cycles).

1 Introduction

The growing energy crisis and environmental problems explored many low-cost, high-performances, environmentally friendly and lightweight energy storage devices like supercapacitors, Li-ion batteries for sustainable and renewable power sources with intensive development [1–4]. In recent years, supercapacitors have attracted considerable attention for emerging energy source applications such as hybrid electric vehicles, portable electronics, regenerating brake systems, etc. due to their favorable features of high power density, fast charge/discharge rates and ultra long cycle life [5]. The charge–discharge properties of supercapacitors are faster than Li-ion batteries and their energy density is much higher than conventional capacitors [3]. The performance of supercapacitors is significantly depends on the properties of electrode materials used. Carbon-based materials and transition metal oxides are extensively used electrode materials for supercapacitors. However, carbon-based materials always suffer from low specific capacitance, which restricts its consumption in growing requirements for renewable energy storage devices and the poor electric conductivity of some transition metal oxides also restricts their practical use for supercapacitors [6]. Therefore, in order to meet the requirement of supercapacitors for large scale practical application, it is highly desirable to explore advanced electrode material, which not only possess high energy density but also good conductivity, improved specific capacitance and excellent chemical stability to fulfill the capable practical application in portable electronic devices and hybrid electric vehicles.

The different kinds of active materials have been developed for supercapacitors, including transition metal oxides like MnO_2, WO_3, MoO_3, V_2O_5, NiO, Co_3O_4 etc. as they possess multiple oxidation states favorable for fast redox reactions and enhances electrochemical performance [6–10]. Among all the transition metal oxides Co_3O_4 is considered as one of the better alternate materials to other hazardous materials due to its environmental friendliness, high theoretical capacitance (3560 F g^{-1}), controllable size and shape, tunable surface and structural properties, good electrochemical performance in alkaline solutions due to its ability to interact with electrolyte ions not only at the surface, but also throughout the bulk, low cost and favorable pseudocapacitive characteristics [10]. Wang et al. [11] reported a specific capacitance of 373 F g^{-1} for Co_3O_4 nanowires at a scan rate of 3 mV s^{-1}. Wang et al. [12] described the hydrothermal synthesis of Co_3O_4 nanorods with a specific capacitance of 281 F g^{-1} at a scan rate of 5 mV s^{-1}. Xia et al. [13]

✉ S. B. Kulkarni
sbk_physics@yahoo.com

1 Department of Physics, The Institute of Science, 15 Madam Cama Road, Mumbai 400032, India

2 Department of Physics, Savitribai Phule University, Pune 411007, India

fabricated hollow Co_3O_4 nanowire arrays by seed mediated hydrothermal method which showed a specific capacitance of 599 F g^{-1} at a constant current density of 2 mV s^{-1}. Thus the reported specific capacitance is less than that of theoretical value of 3560 F g^{-1} to increase the value of specific capacitance Co_3O_4 nanowire is synthesized using chemical method [10]. The nanowire-like morphology have higher charge storage capacity, is attributed to the high surface to volume ratio, plenty of edges, better crystallinity and existence of vacancy-like defects [14].

The present report focuses synthesis of Co_3O_4 nanowires on stainless steel by a simple chemical bath method (CBD). The effects of synthesis parameters and morphology on electrochemical properties of Co_3O_4 nanowires are systematically investigated using cyclic volttametry, galvanostatic charge discharge and electrochemical impedance spectroscopy study. The portable symmetric device of Co_3O_4 nanowires is fabricated and its performance evaluated for energy storage application.

2 Experimental details

2.1 Chemicals

Cobalt nitrate ($Co(NO_3)_2{\cdot}6H_2O$), urea ($CO(NH_2)_2$), and potassium hydroxide (KOH) were purchased from Sigma Aldrich and further purification is not required.

2.2 Synthesis of Co_3O_4 thin film

电化学测

Co_3O_4 thin film was prepared by CBD method. 0.1 M cobalt nitrate [$Co(NO_3)_2{\cdot}6H_2O$] and 0.2 M urea ($CO(NH_2)_2$) was mixed in double distilled water (DDW). The cleaned stainless steel substrates were immersed in reaction bath, which kept at 363 K in constant temperature water bath for 3 h. During the precipitation of solution, heterogeneous reaction occurred on the substrate surface leading to deposition of Co_3O_4 [8]. The substrate coated with Co_3O_4 were removed from reaction bath after 3 h, washed with DDW and dried in hot air [9]. The possible reaction mechanism for synthesis of Co_3O_4 is given bellow,

$$CO(NH_2)_2 + 6H_2O \rightarrow 4NH_3 + 6CH_2O \quad (1)$$

$$2Co^{+} + 4OH^{-} \rightarrow 2Co(OH)_2 \downarrow \quad (2)$$

Firstly, Co^{3+} is produced after $Co(NO_3)_2$ dissolved into distilled water. Urea is an important molecule, which decompose and release OH^- in an indirect manner. Then, Co^{3+} is released and gradually converted into CoOOH via the chemical reaction [15]. The deposited $Co(OH)_2$ thin film further annealed at 623 K to obtain Co_3O_4 .

2.3 Fabrication of Co_3O_4 based symmetric supercapacitor device

To evaluate supercapacitive performance of Co_3O_4 electrodes were deposited on a large area (3×3 cm^{-2}) flexible (SS) substrate. To fabricate symmetric device using Co_3O_4 electrode edges were sealed with adhesive tape to avoid any short. Then, polyvinyl acetate (PVA)/KOH gel electrolyte was painted on Co_3O_4 electrodes and using two electrodes supercapacitor device was assembled. The pressure was applied on supercapacitor device to make good contact.

2.4 Characterization techniques

The structural study of Co_3O_4 thin films were characterized by X-ray diffraction (XRD) (Bruker D8, $\lambda = 1.54$ Å). The surface morphological study of electrode materials was done by field emission scanning electron microscopy (FE-SEM), JEOL JSM 6390. The bounding in Co_3O_4 thin films were studied using Fourier transforms Raman (FT-Raman) spectroscopy. X-ray photoelectron spectroscopy (XPS) was used to detect the oxidation sates of electrodes on Thermo Scientific, K-Alpha set up. The specific surface area and porosity were determined by Brunauer–Emmett–Teller (BET) analysis. The electrochemical measurement of Co_3O_4 thin film electrodes were carried out in an aqueous solution of 1 M KOH electrolyte using three electrode system consisting of Co_3O_4 thin film, platinum, and standard calomel electrode (SCE) as working, counter, and reference electrodes, respectively. Electrochemical properties of Co_3O_4 thin film and symmetric device were tested using automatic battery cycler (WBCS3000). Electrochemical impedance spectroscopy (EIS) measurement was performed using electrochemical workstation (ZIVE SP 5). +TEM

3 Results and discussion

XRD图顯示了具立方結構的多晶氧化鈷形成

Figure 1a shows a typical XRD pattern of cobalt oxide thin film. The XRD pattern shows the formation of polycrystalline cobalt oxide with cubic structure. It is seen that XRD pattern exhibits a major XRD peak reflection along (220) plane. Other peaks corresponding to (311) and (511) planes are observed with low relative intensity. The absence of any other impurity peak suggests high purity of Co_3O_4. The planes are in good agreement with standard JCPDS data file (Card No: 78-1969) of Co_3O_4. Kadam et al. [16] have obtained polycrystalline Co_3O_4 films by spray pyrolysis method. Shinde et al. [17] obtained nanocrystaline Co_3O_4 films using spray pyrolysis. The crystallite size 46 nm is observed for (220) plane calculated by Scherrer formula [18,

16404 Journal of Materials Science: Materials in Electronics (2018) 29:16401–16409

SEM

TEM

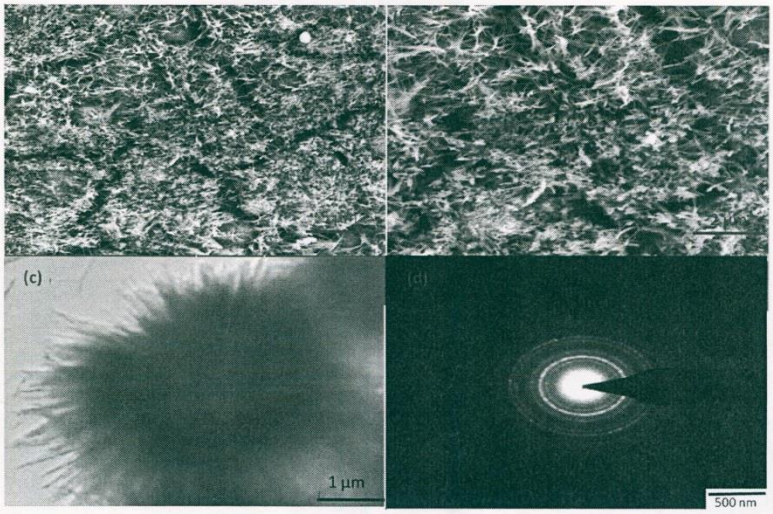

多晶：繞射環
單晶：繞射点

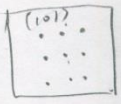

Fig. 3 **a, b** FESEM images at magnifications of ×5000, and ×10,000, respectively and **c, d** TEM image and SAED pattern for Co_3O_4 thin film

TEM micrograph revealed the average diameter of cobalt oxide nanocrystals. The corresponding SAED pattern is shown in Fig. 3d. The blurred bright electron diffraction rings for cobalt oxide film showed that the cobalt oxide film is nanocrystalline. This fact is also supported by the XRD results, where the peak intensities of cobalt oxide film were small. The FESEM study is further supported by BET surface area analysis as shown in Fig. 4.

Co_3O_4 nanowire is characterized by BET measurement. The powder sample is collected from stainless steel Co_3O_4 thin film. The energy density of supercapacitors greatly depends on available specific surface area and proper pore size distribution as it provides more active sites for electrolyte ions for intercalation and de-intercalation during electrochemical redox reactions. Figure 4 presents N_2 adsorption–desorption isotherms for Co_3O_4 sample and insect of Fig. 4 shows Barrett–Joyner–Halenda pore size distribution plot. The N_2 adsorption–desorption isotherms for Co_3O_4 sample displays type IV isotherm. The pore size distribution for Co_3O_4 sample is in the range of 1–10 nm with mean radius of 1.43 nm, which is useful for diffusion and transportation of electrolyte ions and offer enormous electrochemically active sites [21]. The observed surface area for Co_3O_4 is 66.33 $m^2\ g^{-1}$. Xiong et al. [22] reported a BET surface area of 25.12 $m^2\ g^{-1}$ for Co_3O_4 nanosheets. Meher and Rao [23] reported the synthesis of mesoporous

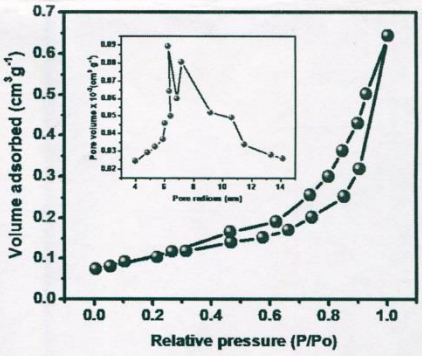

Fig. 4 Nitrogen adsorption–desorption isotherm and inset show pore size distribution for Co_3O_4 thin film

BET 圖無法直接看出，需從电腦結构統計

Co_3O_4 nanowires with BET surface area of 60 $m^2\ g^{-1}$. BET surface area value obtained for the nanowires in the present study is higher than these reported values. This high value of surface area is favorable for better supercapacitor performance of the composites.

Journal of Materials Science: Materials in Electronics (2018) 29:16401–16409 16403

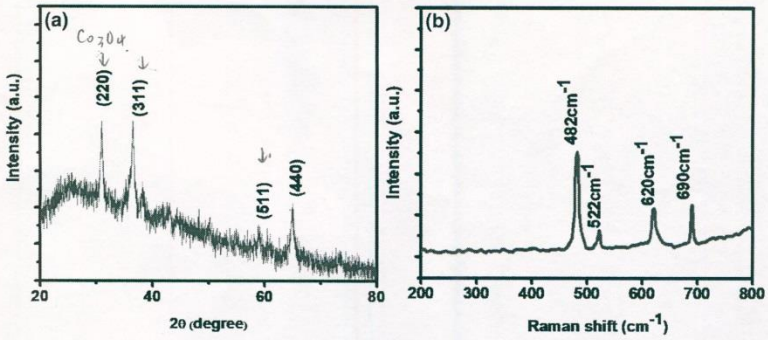

Fig. 1 **a** XRD pattern and, **b** Raman spectrum of Co_3O_4 thin film

19]. The Raman scattered light was collected to form a file containing a Raman spectrum for each individual sample point. The computer is programmed to make a map of the surface. This map showed the intensity of a given Raman peak at each point. The Raman spectrum was measured between the limit of 200–800 cm^{-1} for the cobalt oxide films is shown in Fig. 1b. The peaks marked by arrow at 482 and 690 cm^{-1} are for cobalt oxide [20].

Figure 2a, b shows XPS spectra of Co_3O_4 thin film. Figure 2a shows the satellite peaks observed at 784.2 belonged to Co $2p_{1/2}$ and at 798.1 and 803.3 are belongs to Co $2p_{3/2}$ [13]. Co 2p has peaks at 784.2 eV which indicates Co^{2+} cation species [14]. The two weak satellite peaks at 798.1 and 803.3 belongs to Co^{3+}, which further confirms formation of Co_3O_4. Figure 2b shows O 1s spectrum is fixed by three Gaussian peaks. The peak centered at 531.2 eV is attributed to oxygen in Co_3O_4 phase. O_{ads} peak at 531.2 eV is assigned to surface adsorption oxygen (O^-, O_2^- or O^{2-}) species. The peak at 533.3 eV is generally accredited to adsorbed water or surface carbonate [15].

Figure 3a, b shows the surface morphology of Co_3O_4 thin film at magnifications of ×5000, and ×10,000. FESEM images revealed that the formation of porous nanowires-like structure of Co_3O_4 thin film. This nanowire-like morphology is useful for supercapacitor application. Figure 3c, d shows transmission electron micrograph (TEM) and corresponding selected area electron diffraction (SAED) pattern of cobalt oxide film. From Fig. 3c it shows that the film is composed of agglomeration of nanocrystals which confirms the nanocrystalline nature of annealed cobalt oxide films.

團聚

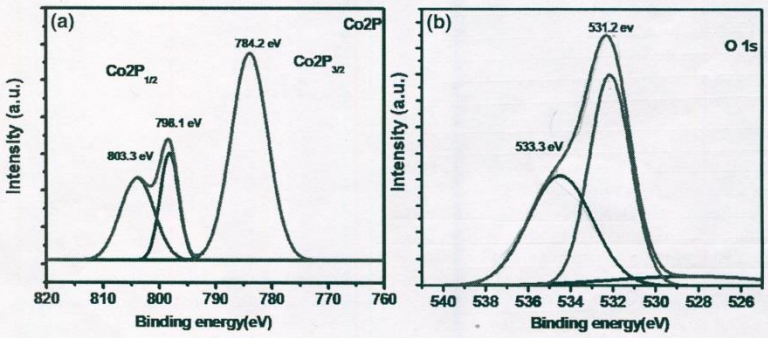

Fig. 2 XPS spectrum of **a** Co 2p, and **b** O 1s core levels of Co_3O_4 thin film

observed in the CV curves of Co_3O_4 which results from reversible transition among Co_3O_4, CoOOH, and CoO_2. The corresponding redox reactions are given below [24].

$$Co_3O_4 + OH^- + H_2O \leftrightarrow 3CoOOH + e^- \quad (3)$$

$$CoOOH + OH^- \leftrightarrow CoO_2 + H_2O + e^- \quad (4)$$

The specific capacitance according to CV curves at different scan rate is calculated from the following formula,

$$C_s = \frac{1}{mv\,(V_{max} - V_{min})} \int_{v_{min}}^{v_{max}} I(V)\,dv \quad (5)$$

where C_s is the specific capacitance (F g^{-1}), m is the mass of deposited material (g), $V_{max} - V_{min}$ is the potential window (V), I is the average current for unit area dipped in the electrolyte. Figure 5b represents the specific capacitance according to CV curves at different scan rates. The maximum specific capacitance of 850 F g^{-1} is obtained at scan rate of 5 mV s^{-1}. It is observed that the Cs of Co_3O_4 nanowire decreases with the increase of scan rates from 5 to 100 mV s^{-1}. The Cs observed for is higher than that of Co_3O_4 nanowire synthesized by hydrothermal method [12, 13]. This is mainly due to the insufficient charge transfer and limited diffusion of electrolyte at active electrode material which is not adequate to satisfy the electrochemical reactions at higher scan rates [20].

The GCD measurement is further performed to get more information about electrochemical properties Co_3O_4 electrode. Figure 5c presents GCD curves of Co_3O_4 electrode at different current densities of 2, 4 and 6 mA cm^{-2}. The discharge curves deviate considerably from the straight line, which indicates that capacitance is mainly due to the faradic redox reactions, suggesting typical pseudocapacitive characteristic of Co_3O_4 electrode [11]. The specific capacitance from discharge curves for different current densities is calculated from following equation,

$$C_s = \frac{I_d \times T_d}{\Delta V \times m} \quad (6)$$

where ΔV is the potential (V), I_d is the discharge current density (mA cm^{-2}) and T_d is discharge time (s). The plot of specific capacitance at different discharge current density is shown in Fig. 5d. The maximum specific capacitance of 825 F g^{-1} is obtained at a current density of 2 mA cm^{-2}. The specific capacitance gradually decreases with the increase of discharge current density. This is due to the increase of potential drop and only outer active material involved in electrochemical redox reactions at higher current densities [21]. This clears that Co_3O_4 electrode demonstrate superior rate capability, revealing its potential for supercapacitor application.

The long-term cycling stability is essential requirement for practical application of supercapacitor. Therefore, the cycling stability of Co_3O_4 electrode is tested in the potential range of −0.2 to +0.45 V/SCE at a scan rate of 100 mV s^{-1} by repeating 5000th CV cycles. The corresponding CV curves for 1st, and 5000th cycles are depicted in of Fig. 5e. Figure 5f shows that Co_3O_4 electrode exhibits capacity retention of 86% over 5000th CV cycles. The CV curve for 5000th does not show change in shape which reveals excellent electrochemical stability with good rate capability. Overall, the superior electrochemical properties of Co_3O_4 electrode are mainly due to the unique hybrid structure with large specific surface area and mesoporosity that facilitate charge transport process more prominently. The open structure of this Co_3O_4 nanowire is excellent for easy accession of electrolyte ions and electron transport during electrochemical reactions. Also, the direct growth of nanowire on stainless steel without use of binder and additives reduces the other undesirable interfaces and defects in the nanostructure [22]. This ensures the utilization of all active material in the electrochemical redox reactions, thus enhancing the electrochemical performance.

EIS technique is used to understand the electrochemical behavior of an electrode material in an electrolyte. A Nyquist plot is the plot of the imaginary component (Z″) of the impedance against the real component (Z′) in the frequency range of 1 Hz–1 MHz, as shown in Fig. 6a. The Nyquist plot shows a small semicircle at higher frequency regions, which can be attributed to the charge transfer process [23]. The equivalent series resistance (ESR) is calculated from the X-intercept of Nyquist plot, and ESR of Co_3O_4 electrodes is 0.7 Ω. At the low frequency range, the straight line nature is attributed to the ion diffusion in the electrolyte is Warburg impedance [24]. It is observed that, R_s, corresponds to the resistance of the electrolyte (0.7 Ω) which is independent of the frequency and R_{ct} is the charge transfer resistance (2.4 Ω). The phase angle at a higher frequency range is inferior because of the ionic resistance of electrolyte corresponds to lower capacitance (Fig. 6a). Phase angle reaches toward −90° at lower frequency range denote capacitive behavior of Co_3O_4 electrode (Fig. 6b). Overall performance of Co_3O_4 electrode shows promising positive electrode material for SSSCs device.

3.2 Electrochemical properties of Co_3O_4 symmetric solid-state (SSS) supercapacitor device

Figure 7a shows the effect of scan rate on supercapacitor properties of Co_3O_4 SSS device is studied within the potential window of −0.8 to +0.8 V. The current density under curve CV curves is slowly increased with scan rate [25]. This shows that voltammetric current is directly proportional to scan rate of CV, which is one of pesdocapacitive behavior

Journal of Materials Science: Materials in Electronics (2018) 29:16401–16409

3.1 Electrochemical properties of Co_3O_4 electrode

Furthermore, to evaluate electrochemical behavior of Co_3O_4 electrodes for supercapacitors, cyclic voltammetry (CV) and galvanostatic charge–discharge (GCD) measurements were performed in 1 M KOH aqueous solution using conventional three electrode system at room temperature. Figure 5a shows the CV measurement of Co_3O_4 electrodes in a potential window of from −0.2 to +0.45 V/SCE at scan rates of 5–100 mV s^{-1}, respectively. The area integrated inside CV curves increases with the increase with scan rate. The CV curves of Co_3O_4 electrode shows peaks in curves which indicate psudocapacitive nature of Co_3O_4 electrode [15]. From CV curves it is seen that the area under the curves increases with the increase of scan rate from 5 to 100 mV s^{-1}. Two sets of redox peaks were

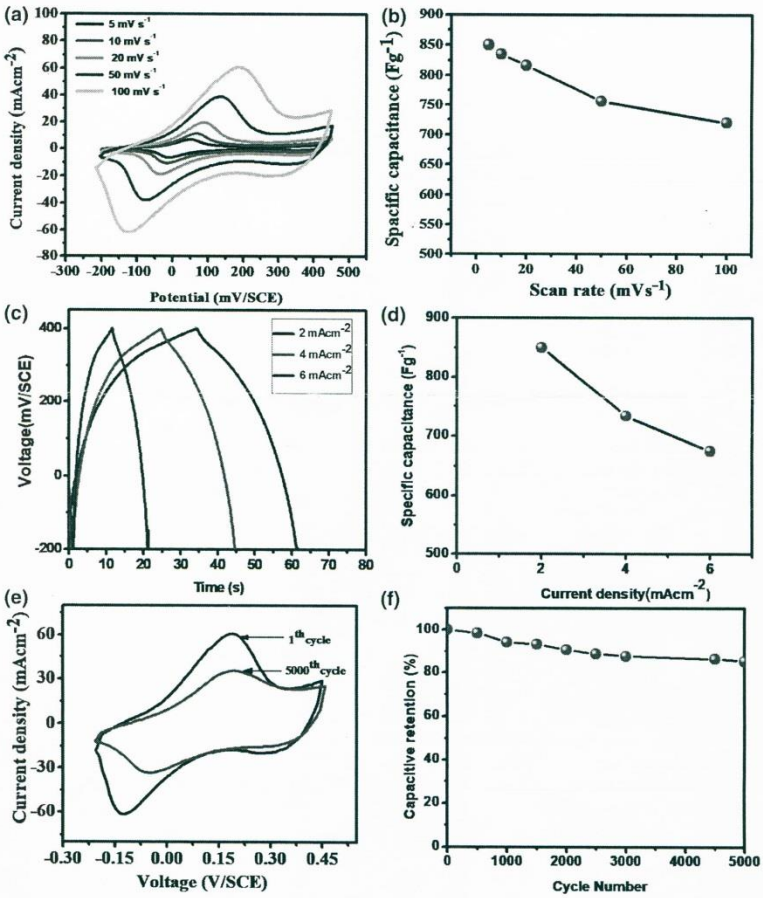

Fig. 5 **a** CV curves at various scan rate, **b** variation of specific capacitance with scan rate, **c** GCD curves at various current density, **d** variation of specific capacitance with different current density, **e** stability study at 100 mV s^{-1} scan rate, **f** capacitive retention at different cycle number of Co_3O_4 thin film

Journal of Materials Science: Materials in Electronics (2018) 29:16401–16409

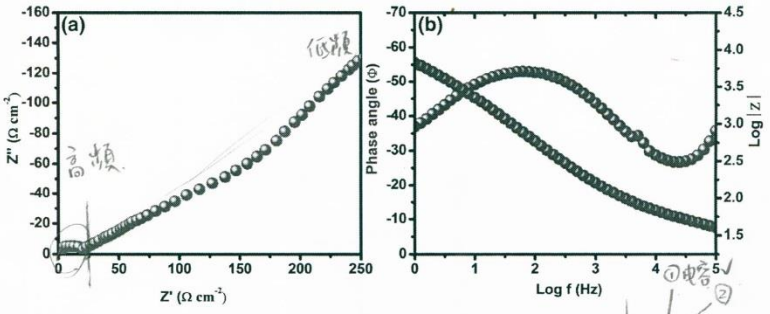

Fig. 6 **a** Nyquist plot and, **b** Bode plots of phase angle (Φ) and log |Z| versus log f for Co_3O_4 thin film

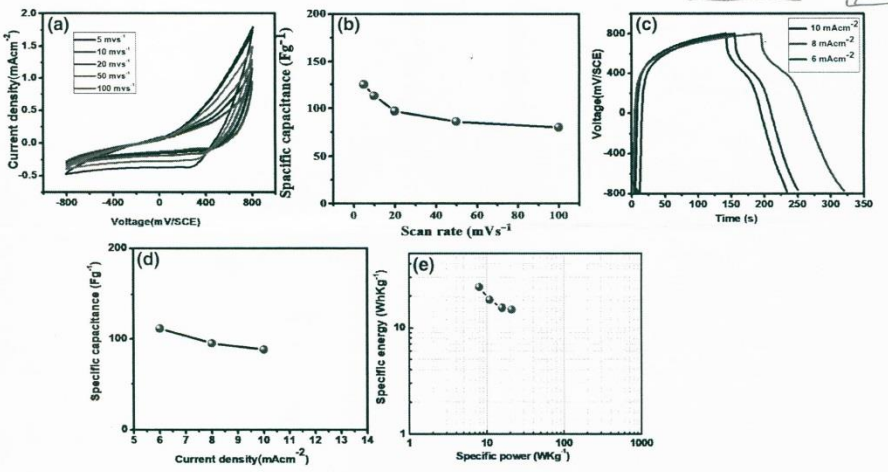

Fig. 7 **a** CV curves at various scan rate, **b** variation of specific capacitance with scan rate, **c** GCD curves at various current density, **d** variation of specific capacitance with different current density, **e** Ragon plot for Co_3O_4 SSS device

[26]. The variation of specific capacitance with scan rate is shown in Fig. 7b which reveals that Co_3O_4 SSS device exhibit maximum C_s of 127 F g^{-1} at scan rate of 5 mV s^{-1}. The high C_s value is observed due to nanowires-like morphology of Co_3O_4 electrode [27].

GCD study for Co_3O_4 SSS device is performed at different current density within constant potential window of −0.8 to 0.8 V. Figure 7c shows GCD curve divided in to two parts, 1st is resistive part arises due to the sudden voltage drop shows internal resistance (IR), and second part is capacitive related to voltage change with respect to change in energy within the capacitor [28]. The C_s of symmetric device is 112 F g^{-1} at current density of 6 mA. The change in C_s of symmetric device with current density is shown Fig. 7d. Ragone plot of specific energy (SP) and specific power (SE) is shown in Fig. 7e. Evaluated values of specific energy and specific power for Co_3O_4 SSS device are 24.18 Wh kg^{-1}, and 8.50 W kg^{-1}. Figure 8a shows the cyclic stability of Co_3O_4 SSS device at scan rate of 100 mV s^{-1} for 3000th cycles. Co_3O_4 based SSS device shows stability of 85% over 3000 cycles (Fig. 8b).

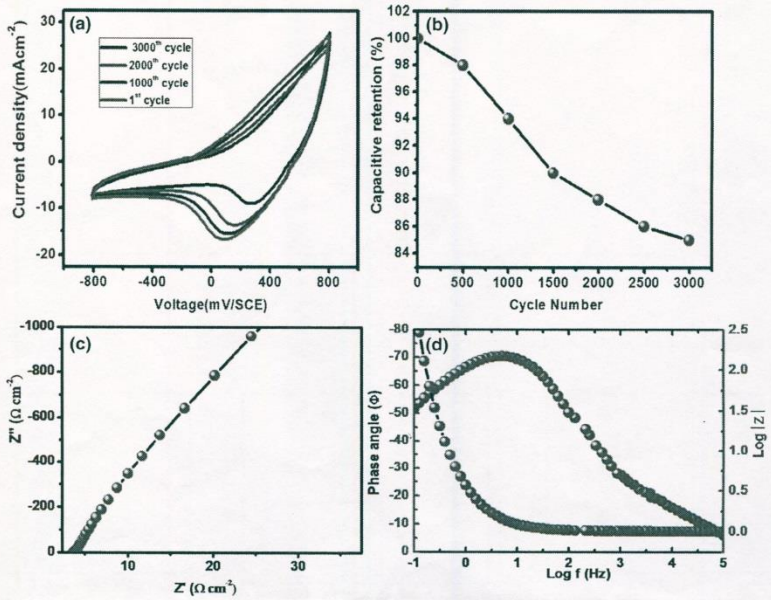

Fig. 8 **a** Stability study at 100 mV s^{-1} scan rate, **b** capacitive retention at different cycle number, **c** Nyquist plot and, **d** Bode plots of phase angle (Φ) and log |Z| versus log f for Co_3O_4 SSS device

It indicates that the material behave reversibly as an excellent capacitor material for large number of cycles [29].

EIS technique is used to study the electrochemical behavior of Co_3O_4 SSS device. Figure 8c shows Nyquist plot consisting of imaginary impedance component (Z″) against the real impedance component (Z′) in the frequency range from 1 Hz to 1 MHz for Co_3O_4 SSS device. Nyquist plot obtained is divided in to low and high frequency regions. In the high frequency region, it shows indistinct semi-circle indicating good supercapacitive behavior [30]. The observed equivalent series resistance (R_s) and charge transfer resistance (R_{ct}) of 1.85 and 1.34 Ω cm^{-2}, respectively are determined from Nyquist plot. Figure 8d shows Bode plots which show the phase angle of 62°. The phase angle tends to 90° confirms supercapacitor behavior of Co_3O_4 SSS device [31].

4 Conclusions

The nanowires-like structure of Co_3O_4 thin film is deposited on stainless steel substrate with simple chemical bath deposition route at different deposition temperatures. Co_3O_4 thin film deposited at 363 K shows high crystallanity, and nanowires-like morphology, which is useful in energy storage application. The electrochemical storage performance of Co_3O_4 electrode is studied in 1 M KOH electrolyte which shows high specific capacitance of 850 F g^{-1} at 5 mV s^{-1}. The symmetric supercapacitor device shows high energy density of 24.18 Wh kg^{-1}.

Acknowledgements Dr. A. A.Yadav is thankful to Science and Engineering Research Board, New Delhi, for the financial support and awarding National Postdoctoral Fellowship (N-PDF) award F. No. PDF/2017/001419. Dr. Y. M. Hunge is thankful to Science and Engineering Research Board, New Delhi, for the financial support and awarding National Postdoctoral Fellowship (N-PDF) award F. No. PDF/2017/000691.

References

1. Z. Wu, Y. Zhu, X. Ji, J. Mater. Chem. A **2**, 14759 (2014)
2. S.C. Pang, M.A. Anderso, T.W. Chapman, J. Electrochem. Soc. **147**, 44 (2000)
3. A.A. Yadav, A.C. Lokhande, R.B. Pujari, J.H. Kim, C.D. Lokhande, J. Colloid Interface Sci. **51**, 484 (2016)

4. G. Wang, L. Zhang, J. Zhang, Chem. Soc. Rev. **47**, 797 (2012)
5. Q. Liao, N. Li, S. Jin, G. Yang, C. Wang, ACS Nano **9**, 5310 (2015)
6. S. Mitra, A.K. Shukla, S. Sampath, J. Power Sources **101**, 213 (2001)
7. C.Z. Yang, F. Xu, W. Zhang, Z. Mei, B. Pei, X. Zhu, J. Power Sources **24**, 246 (2014)
8. D. Pech, M. Brunet, H. Durou, P. Huang, V. Mochalin, Y. Gogotsi, P.L. Taberna, P. Simon, Nat. Nanotechnol. **5**, 651 (2010)
9. K.W. Nam, J.B. Kim, J. Electrochem. Soc. **149**, 346 (2002)
10. R.B. Rakhi, W. Chen, D. Cha, H.N. Alshareef, Nano Lett. **12**, 2559 (2012)
11. L.L. Wang, X. Wang, X. Yang, L. Lu, J. Mater. Sci.: Mater. Electron. **22**, 601 (2011)
12. G.X. Wang, X.P. Shen, J. Horvat, B. Wang, H. Liu, D. Wexler, J. Yao, J. Phys. Chem. C **113**, 4357 (2009)
13. X.H. Xia, J.P. Tu, Y.J. Mai, X.L. Wang, C.D. Gu, X.B. Zhao, J. Mater. Chem. **21**, 9319 (2011)
14. S. Ghosh, S.R. Polaki, M. Kamruddin, S.M. Jeong, K. Ostrikov, J. Phys. D **51**, 145303 (2018)
15. R.K. Chava, S.Y. Oh, Y.T. Yu, CrystEng Comm **18**, 3655 (2018)
16. L.D. Kadam, P.S. Patil, Mater. Chem. Phys. **68**, 225 (2001)
17. V.R. Shinde, S.B. Mahadik, T.P. Gujar, C.D. Lokhande, App. Surf. Sci. **252**, 7487 (2006)
18. Y.M. Hunge, A.A. Yadav, B.M. Mohite, V.L. Mathe, C.H. Bhosale, J. Mater. Sci.: Mater. Electron. **29**, 3808 (2018)
19. Y.M. Hunge, A.A. Yadav, V.L. Mathe, J. Mater. Sci.: Mater. Electron. **29**, 6183 (2018)
20. O. Bockman, T. Ostvold, G.A. Voyiatzis, G.N. Papatheodorou, Hydrometallurgy **55**, 93 (2000)
21. Y.M. Hunge, MOJ Polym. Sci. **1**, 00020 (2017)
22. S. Xiong, C. Yuan, X. Zhang, B. Xi, Y. Qian, Chem. Eur. J. **15**, 5320 (2009)
23. S.K. Meher, G.R. Rao, J. Phys. Chem. C **115**, 15646 (2011)
24. R. Tummala, R.K. Guduru, P.S. Mohanty, J. Power Sources **209**, 44 (2012)
25. A.A. Yadav, A.C. Lokhande, J.H. Kim, Int. J. Hydrog. Energy **41**, 18311 (2016)
26. I.G. Casella, M. Gatta, J. Electroanal. Chem. **534**, 31 (2002)
27. H. Zheng, F. Tang, M. Lim, A. Mukherji, H. Yan, L. Wang, G. Lu, J. Power Sources **195**, 680 (2010)
28. A.A. Yadav, A.C. Lokhande, J.H. Kim, C.D. Lokhande, J. Colloid Interface Sci. **443**, 22 (2016)
29. S.B. Kulkarni, V.S. Jamadade, D.S. Dhawale, C.D. Lokhande, Appl. Surf. Sci. **255**, 8390 (2009)
30. A.A. Yadav, A.C. Lokhande, J.H. Kim, C.D. Lokhade, J. Ind. Eng. Chem. **56**, 90 (2017)
31. R.B. Pujari, A.C. Lokhande, A.A. Yadav, J.H. Kim, C.D. Lokhande, Mater. Des. **108**, 510 (2016)

6.4 書面報告其他參考文獻

1. Yadav, A.A., Y.M. Hunge, and S.B. Kulkarni, *Chemical synthesis of Co3O4 nanowires for symmetric supercapacitor device.* Journal of Materials Science: Materials in Electronics, 2018. **29**(19): p. 16401-16409.
2. Zhang, G., et al., *Nanoforest of hierarchical Co3O4@NiCo2O4 nanowire arrays for high-performance supercapacitors.* Nano Energy, 2013. **2**(5): p. 586-594.
3. Xiong, Q., et al., *Reconstruction of TiO2/MnO2-C nanotube/nanoflake core/shell arrays as high-performance supercapacitor electrodes.* Nanotechnology, 2016. **28**(5): p. 055405.
4. Pawar, S.M., et al., *Nanoporous CuCo2O4 nanosheets as a highly efficient bifunctional electrode for supercapacitors and water oxidation catalysis.* Applied Surface Science, 2019. **470**: p. 360-367.
5. Cai, D., et al., *High-Performance Supercapacitor Electrode Based on the Unique ZnO@Co3O4 Core/Shell Heterostructures on Nickel Foam.* ACS Applied Materials & Interfaces, 2014. **6**(18): p. 15905-15912.
6. Xia, X.-h., et al., *Freestanding Co3O4 nanowire array for high performance supercapacitors.* RSC Advances, 2012. **2**(5): p. 1835-1841.
7. *<nchu-103-7101065040-1.pdf>.*
8. Xia, X.-h., et al., *Self-supported hydrothermal synthesized hollow Co3O4 nanowire arrays with high supercapacitor capacitance.* Journal of Materials Chemistry, 2011. **21**(25): p. 9319-9325.
9. 林逸傑, *化學浴沉積法製備孔洞性四氧化三鈷奈米片薄膜應用於一氧化碳氣體感測之特性研究*, in *材料科學與工程系所*. 2014, 交通大學. p. 1-111.
10. Wang, H. and L. Pilon, *Physical interpretation of cyclic voltammetry for measuring electric double layer capacitances.* Electrochimica Acta, 2012. **64**: p. 130-139.
11. Brunauer, S., P.H. Emmett, and E. Teller, *Adsorption of Gases in Multimolecular Layers.* Journal of the American Chemical Society, 1938. **60**(2): p. 309-319.
12. Thommes, M., et al., *Physisorption of gases, with special reference to the evaluation of surface area and pore size distribution (IUPAC Technical Report).* Pure and Applied Chemistry, 2015. **87**(9-10): p. 1051-1069.
13. Xiong, S., et al., *Controllable synthesis of mesoporous Co3O4 nanostructures with tunable morphology for application in supercapacitors.* Chemistry, 2009. **15**(21): p. 5320-6.

14. Meher, S.K. and G.R. Rao, *Effect of Microwave on the Nanowire Morphology, Optical, Magnetic, and Pseudocapacitance Behavior of Co3O4.* The Journal of Physical Chemistry C, 2011. **115**(51): p. 25543-25556.
15. Meher, S.K. and G.R. Rao, *Ultralayered Co3O4 for High-Performance Supercapacitor Applications.* The Journal of Physical Chemistry C, 2011. **115**(31): p. 15646-15654.

6.5 其他重要參考文獻節錄

CHEMISTRY
A EUROPEAN JOURNAL

DOI: 10.1002/chem.200802671

Controllable Synthesis of Mesoporous Co_3O_4 Nanostructures with Tunable Morphology for Application in Supercapacitors

Shenglin Xiong,[a] Changzhou Yuan,[b] Xiaogang Zhang,[b] Baojuan Xi,[a] and Yitai Qian*[a]

Figure 6. High-resolution XPS measurements for the Co 2p (a) and O 1s (b) core levels for the Co_3O_4 nanosheets.

about 0.46 nm corresponds to the value of the (111) plane of cubic Co_3O_4, which is in agreement with the powder XRD result.

To investigate the specific surface areas and the porous nature of the Co_3O_4 nanosheets and microspheres further, Brunauer–Emmett–Teller (BET) gas-sorption measurements were performed. Nitrogen adsorption–desorption isotherms of these porous nanostructures are shown in Figure 8, and the insets illustrate the corresponding Barrett–Joyner–Halenda (BJH) pore size distribution plots. These isotherms can be categorized as type IV, with a distinct hysteresis loop observed in the range 0.5–1.0 p/p_o (Figure 8). The BET specific surface areas and micropore areas of the samples were 25.12 and 2.80 $m^2 g^{-1}$ for the Co_3O_4 nanosheets and 21.53 and 1.29 $m^2 g^{-1}$ for the Co_3O_4 microspheres, respectively, which shows that there is clearly a difference in the specific surface area and the micropore area between the two types of morphology. The average pore diameters were 26.7 and 23.5 nm, respectively, according to the BJH plots calculated from the nitrogen isotherms of the porous Co_3O_4 nanosheets and microspheres and indicate that all of the samples contain mesoscale pores. The results are in good agreement with the value determined by the high-magnification TEM observations discussed above. The mesoporous Co_3O_4 nanostructures could reduce transport limitation in catalysis, leading to higher activities and well-controlled selectivity, and have potential applications in the field of surface catalysis.

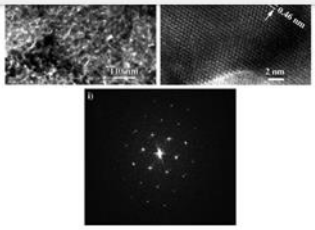

Figure 7. a)–d) FESEM images of mesopore Co_3O_4 nanosheets, e) and f) FESEM images of mesopore Co_3O_4 microspheres, g) a high-magnification TEM image of a single Co_3O_4 nanosheet, and h) and i) the corresponding high-resolution transmission electron microscopy (HRTEM) and fast Fourier transform electron diffraction (FFTED) pattern of the individual mesoporous Co_3O_4 nanosheet.

THE JOURNAL OF PHYSICAL CHEMISTRY C
ARTICLE
pubs.acs.org/JPCC

Effect of Microwave on the Nanowire Morphology, Optical, Magnetic, and Pseudocapacitance Behavior of Co_3O_4

Sumanta Kumar Meher and G. Ranga Rao*

Department of Chemistry, Indian Institute of Technology Madras, Chennai 600036, India

Supporting Information

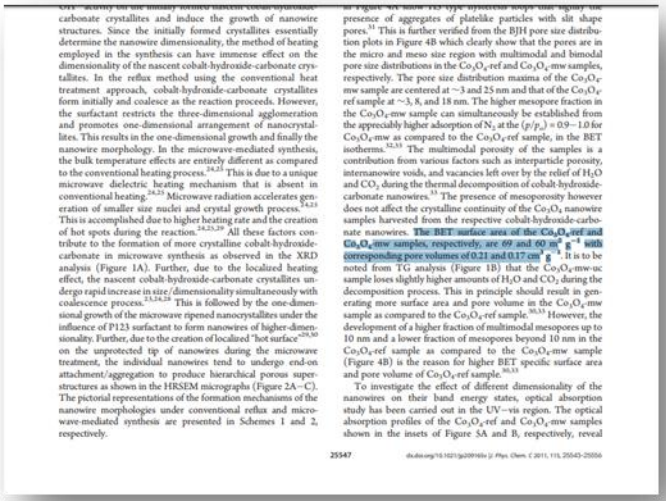

carbonate crystallites and induce the growth of nanowire structures. Since the initially formed crystallites essentially determine the nanowire dimensionality, the method of heating employed in the synthesis can have immense effect on the dimensionality of the nascent cobalt-hydroxide-carbonate crystallites. In the reflux method using the conventional heat treatment approach, cobalt-hydroxide-carbonate crystallites form initially and coalesce as the reaction proceeds. However, the surfactant restricts the three-dimensional agglomeration and promotes one-dimensional arrangement of nanocrystallites. This results in the one-dimensional growth and finally the nanowire morphology. In the microwave-mediated synthesis, the bulk temperature effects are entirely different as compared to the conventional heating process.[24,25] This is due to a unique microwave dielectric heating mechanism that is absent in conventional heating.[24,25] Microwave radiation accelerates generation of smaller size nuclei and crystal growth process.[24,25] This is accomplished due to higher heating rate and the creation of hot spots during the reaction.[24,25,29] All these factors contribute to the formation of more crystalline cobalt-hydroxide-carbonate in microwave synthesis as observed in the XRD analysis (Figure 1A). Further, due to the localized heating effect, the nascent cobalt-hydroxide-carbonate crystallites undergo rapid increase in size/dimensionality simultaneously with coalescence process.[23,24,28] This is followed by the one-dimensional growth of the microwave ripened nanocrystallites under the influence of P123 surfactant to form nanowires of higher-dimensionality. Further, due to the creation of localized "hot surface"[29,30] on the unprotected tip of nanowires during the microwave treatment, the individual nanowires tend to undergo end-on attachment/aggregation to produce hierarchical porous superstructures as shown in the HRSEM micrographs (Figure 2A−C). The pictorial representations of the formation mechanisms of the nanowire morphologies under conventional reflux and microwave-mediated synthesis are presented in Schemes 1 and 2, respectively.

presence of aggregates of platelike particles with slit shape pores.[31] This is further verified from the BJH pore size distribution plots in Figure 4B which clearly show that the pores are in the micro and meso size region with multimodal and bimodal pore size distributions in the Co_3O_4-ref and Co_3O_4-mw samples, respectively. The pore size distribution maxima of the Co_3O_4-mw sample are centered at ~3 and 25 nm and that of the Co_3O_4-ref sample at ~3, 8, and 18 nm. The higher mesopore fraction in the Co_3O_4-mw sample can simultaneously be established from the appreciably higher adsorption of N_2 at the $(p/p_0) = 0.9-1.0$ for Co_3O_4-mw as compared to the Co_3O_4-ref sample, in the BET isotherms.[32,33] The multimodal porosity of the samples is a contribution from various factors such as interparticle porosity, internanowire voids, and vacancies left over by the relief of H_2O and CO_2 during the thermal decomposition of cobalt-hydroxide-carbonate nanowires.[33] The presence of mesoporosity however does not affect the crystalline continuity of the Co_3O_4 nanowire samples harvested from the respective cobalt-hydroxide-carbonate nanowires. The BET surface area of the Co_3O_4-ref and Co_3O_4-mw samples, respectively, are 69 and 60 $m^2 g^{-1}$ with corresponding pore volumes of 0.21 and 0.17 $cm^3 g^{-1}$. It is to be noted from TG analysis (Figure 1B) that the Co_3O_4-mw-ac sample loses slightly higher amounts of H_2O and CO_2 during the decomposition process. This in principle should result in generating more surface area and pore volume in the Co_3O_4-mw sample as compared to the Co_3O_4-ref sample.[30,33] However, the development of a higher fraction of multimodal mesopores up to 10 nm and a lower fraction of mesopores beyond 10 nm in the Co_3O_4-ref sample as compared to the Co_3O_4-mw sample (Figure 4B) is the reason for higher BET specific surface area and pore volume of Co_3O_4-ref sample.[30,33]

To investigate the effect of different dimensionality of the nanowires on their band energy states, optical absorption study has been carried out in the UV−vis region. The optical absorption profiles of the Co_3O_4-ref and Co_3O_4-mw samples shown in the insets of Figure 5A and B, respectively, reveal

25547 dx.doi.org/10.1021/jp209169z |J. Phys. Chem. C 2011, 115, 25543–25556

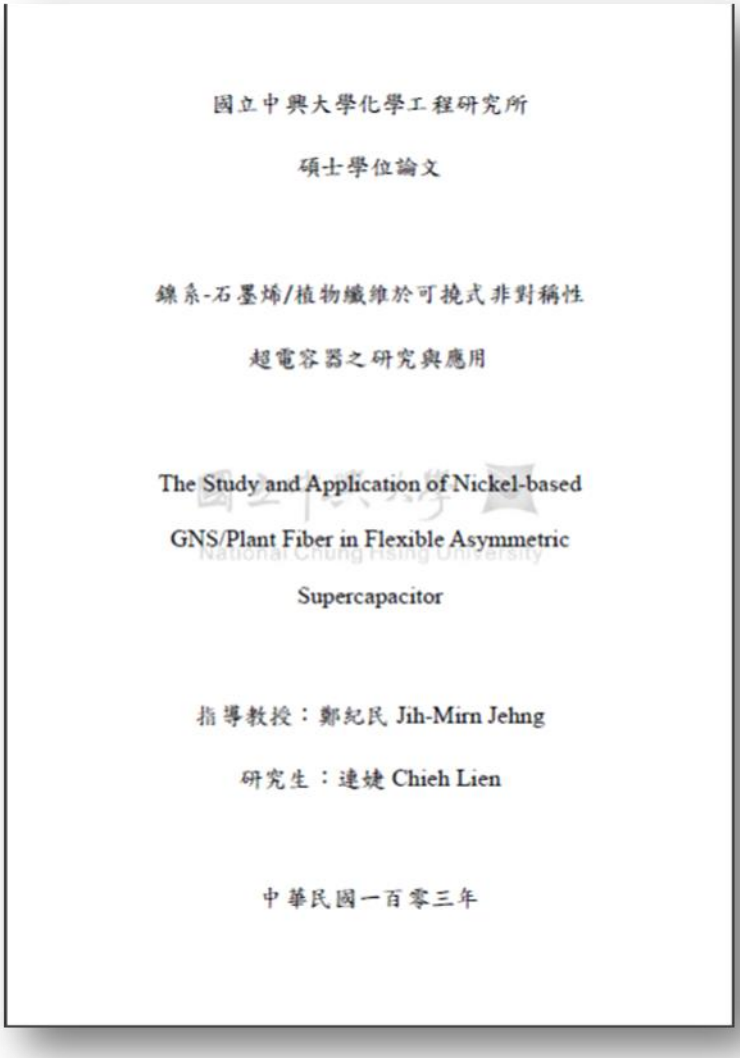

國立中興大學化學工程研究所

碩士學位論文

鎳系-石墨烯/植物纖維於可撓式非對稱性

超電容器之研究與應用

The Study and Application of Nickel-based

GNS/Plant Fiber in Flexible Asymmetric

Supercapacitor

指導教授：鄭紀民 Jih-Mirn Jehng

研究生：連婕 Chieh Lien

中華民國一百零三年

第二章文獻回顧

2-1 超級電容器

2-1-1 超級電容器簡介

超級電容器又稱為電化學電容器(Electrochemical Capacitors)或超高電容器(Ultracapacitors)，是由電極材料、電解液、集電器等組合而成，如圖2-1-1-1，電極材料的特質是決定超級電容器的關鍵因素，優異的電容行為通常與電極材料的高比表面積或高度可逆的氧化還原反應活性有關，電解液則是決定其操作電壓的範圍，做為一個儲電裝置，超級電容器的電容一般可達到F的等級(farad)，而傳統電容器的儲電量約只有mF(millifarad)，可藉由此做為超級電容器與傳統電容器的分界線[15]。

超級電容器或稱用來取代電池，而是與電池相互結合，或是在低能量需求的應用取代電池做為電力來源，理想狀況為超級電容器與電池相互結合，需要高瞬間功率時，由超級電容器瞬間釋放出，通常依據所使用的電力需求，在高輸出功率以及短運作時間的情況下，採用電雙層電容器做為電力來源或電力輔助，若是要求高放電能力及高能量儲存以及輸出時，適合法拉第擬電容器做為儲能元件[15]。

總體來說，超級電容器可以分成以下幾種類型，超電容器的分類樹狀圖如圖2-1-1-2表示。

（1）由電極材料儲能機構的不同，可以分成電雙層以及法拉第擬電容器。

（2）依據超級電容器組成結構的不同，可以分成對稱型以及非對稱型超級電容器。

（3）根據電解液的不同，可以分成水溶液電解液超電容器以及

2-1-2電極材料儲能機構的影響

（1）電雙層電容器(Electric Double Layer Capacitor EDLC)

電解質中之陰陽電離子在電極與電解液之間的介面，透過定向排列，形成電位差來產生電容[17]，如圖2-1-2-1所示，充電時，陰陽離子分別往正負極移動，在電極表面形成雙電層，電解質離子到達電極表面，但是並不與之反應或是吸附在其上，是靠靜電吸引力造成電荷分離，來儲存電能。電極的比電容值是由電極比表面積、電解質種類以及有效的電雙層厚度所決定[18]，因此若是電極材料能與電解質有超好的接觸，所得到的比電容值會越高，電雙層電容器之循環伏安法的特性圖沒有明顯的氧化還原波峰，而是呈現出矩形的形狀，若是其形態與矩形越是接近，代表越良好的電雙層效應，而矩形中面積越大則代表電極比電容值越大，以電雙層材料做為超電容器之電極，有什麼穩定的優勢。

碳質材料是現今應用最多層面，商業化最成熟的電極材料，它們來源廣泛，其孔徑可變化性以及形態多樣等優點，常使用的材料例如活性碳(Activated Carbons)、石墨烯(Graphene)、碳凝膠(Carbon Aerogels) [15]等，具有良好的電學性質，其中石墨烯的發展為超級電容器的儲能帶來了新的方向，由於石墨烯特有的高導電率使具有高比電容值，並且擁有sp^2共價鍵形成之二維平面結構，能設計出不同結構和性能之基材。

（2）法拉第擬電容器（Pseudo-capacitor）

利用電極中的活性物質，如金屬氧化物或是導電高分子等，進行氧化還原反應，由於這些反應遵守法拉第定律，也就是電流強與化學反應量成正比，因此稱為法拉第擬電容器，其電化學特性為反應電流

2-1-2電極材料儲能機構的影響

（1）電雙層電容器(Electric Double Layer Capacitor EDLC)

電解質中之陰陽電離子在電極與電解液之間的介面，透過定向排列，形成電位差來產生電容[17]，如圖2-1-2-1所示，充電時，陰陽離子分別往正負極移動，在電極表面形成雙電層，電解質離子到達電極表面，但是並不與之反應或是吸附在其上，是靠靜電吸引力造成電荷分離，來儲存電能。電極的比電容值是由電極比表面積、電解質種類以及有效的電雙層厚度所決定[18]，因此若是電極材料能與電解質有超好的接觸，所得到的比電容值會越高，電雙層電容器之循環伏安法的特性圖沒有明顯的氧化還原波峰，而是呈現出矩形的形狀，若是其形態與矩形越是接近，代表越良好的電雙層效應，而矩形中面積越大則代表電極比電容值越大，以電雙層材料做為超電容器之電極，有什麼穩定的優勢。

碳質材料是現今應用最多層面，商業化最成熟的電極材料，它們來源廣泛，其孔徑可變化性以及形態多樣等優點，常使用的材料例如活性碳(Activated Carbons)、石墨烯(Graphene)、碳凝膠(Carbon Aerogels) [15]等，具有良好的電學性質，其中石墨烯的發展為超級電容器的儲能帶來了新的方向，由於石墨烯特有的高導電率使具有高比電容值，並且擁有sp^2共價鍵形成之二維平面結構，能設計出不同結構和性能之基材。

（2）法拉第擬電容器（Pseudo-capacitor）

利用電極中的活性物質，如金屬氧化物或是導電高分子等，進行氧化還原反應，由於這些反應遵守法拉第定律，也就是電流強與化學反應量成正比，因此稱為法拉第擬電容器，其電化學特性為反應電流

專題討論自我評量表

1. 本學期中我從自己的「專題討論」課程學到什麼？我從班上其他同學身上真正學到什麼特別之處？(請具體描述)

專題討論課是我第一次報告文獻，而且必須用比較科普的方式報告，的確需要費一番功夫準備。與以前的報告相差最多在於，聽眾為同系同學和老師，許多東西不必特別說明，憑大家的基本知識背景也都能理解，因此如何讓我的報告令人感到耳目一新是我在這門課學到的第一件事情。第二件事情是提問，每個同學報告的內容不盡相同，但要如何提問相關問題，是我在這堂課學到最多的，雖然一開始提的問題很沒程度，但隨著提問的次數多了，漸漸知道怎麼提問以及哪些問題能夠問得更深入。

最後，我從班上同學身上學到了一些簡報模板的製作，一些比較好看的背景或排版我都有記下來，希望以後能派上用場。

2. 我個人在「專題討論」表達力方面，有哪些尚須值得改進加強的地方呢？ (請具體描述)

我覺得這堂課比較可惜的是，要自己記下發問次數，有些同學會造假或是有人為了避免自己報告時被提問，而不願意舉手問問題，更讓人覺得不齒的是有些同學嫉妒別人提問的次數較多，在背後詆毀他人，造成提問者心理上壓力而不敢再提問，但背後詆毀別人的同學仍舊在課堂上提問拿分數。

建議可以由老師記錄提問同學和他的提問次數，和取消同學互評，因為有些人雞眼肚腸，若被提問了而答不出就把提問者口頭報告時的分數調低，有失公平性。

3. 我對「專題討論」課程提出一些創新性建議，敘述如下:

我建議可以加快前面幾堂說明的課程，讓同學早一點報告，留下最後一週給自願想要重新報告的同學重新報告。

4. 我這學期中上課出席率(100%)是 100％ 。

5. 我共花費 10 小時準備報告資料，共收集研讀 25 篇中文英文相關資料。

6. 我自評對「專題討論」的個人學習滿意程度為 95 分 (以滿分為 100 分評量) 。

7. 我自評對「專題討論」授課老師教學滿意度為 ___99___ 分 (以滿分為 100 分評量) 。

我的「專題討論」的「書面報告(小論文)」經過圖書館 **Turn It In** 軟體的比對結果所出現的相似度比率為___1___% (後面請附上 **Turn It In** 比對結果的列印資料)

參考文獻

1. Yadav, A.A., Y.M. Hunge, and S.B. Kulkarni, *Chemical synthesis of Co3O4 nanowires for symmetric supercapacitor device.* Journal of Materials Science: Materials in Electronics, 2018. **29**(19): p. 16401-16409.
2. Zhang, G., et al., *Nanoforest of hierarchical Co3O4@NiCo2O4 nanowire arrays for high-performance supercapacitors.* Nano Energy, 2013. **2**(5): p. 586-594.
3. Xiong, Q., et al., *Reconstruction of TiO2/MnO2-C nanotube/nanoflake core/shell arrays as high-performance supercapacitor electrodes.* Nanotechnology, 2016. **28**(5): p. 055405.
4. Pawar, S.M., et al., *Nanoporous CuCo2O4 nanosheets as a highly efficient bifunctional electrode for supercapacitors and water oxidation catalysis.* Applied Surface Science, 2019. **470**: p. 360-367.
5. Cai, D., et al., *High-Performance Supercapacitor Electrode Based on the Unique ZnO@Co3O4 Core/Shell Heterostructures on Nickel Foam.* ACS Applied Materials & Interfaces, 2014. **6**(18): p. 15905-15912.
6. Xia, X.-h., et al., *Freestanding Co3O4 nanowire array for high performance supercapacitors.* RSC Advances, 2012. **2**(5): p. 1835-1841.
7. *<nchu-103-7101065040-1.pdf>.*
8. Xia, X.-h., et al., *Self-supported hydrothermal synthesized hollow Co3O4 nanowire arrays with high supercapacitor capacitance.* Journal of Materials Chemistry, 2011. **21**(25): p. 9319-9325.
9. 林逸傑, *化學浴沉積法製備孔洞性四氧化三鈷奈米片薄膜應用於一氧化碳氣體感測之特性研究*, in *材料科學與工程系所*. 2014, 交通大學. p. 1-111.
10. Wang, H. and L. Pilon, *Physical interpretation of cyclic voltammetry for measuring electric double layer capacitances.* Electrochimica Acta, 2012. **64**: p. 130-139.
11. Brunauer, S., P.H. Emmett, and E. Teller, *Adsorption of Gases in Multimolecular Layers.* Journal of the American Chemical Society, 1938. **60**(2): p. 309-319.
12. Thommes, M., et al., *Physisorption of gases, with special reference to the evaluation of surface area and pore size distribution (IUPAC Technical Report).* Pure and Applied Chemistry, 2015. **87**(9-10): p. 1051-1069.
13. Xiong, S., et al., *Controllable synthesis of mesoporous Co3O4 nanostructures with tunable morphology for application in supercapacitors.* Chemistry, 2009. **15**(21): p. 5320-6.

14. Meher, S.K. and G.R. Rao, *Effect of Microwave on the Nanowire Morphology, Optical, Magnetic, and Pseudocapacitance Behavior of Co3O4.* The Journal of Physical Chemistry C, 2011. **115**(51): p. 25543-25556.
15. Meher, S.K. and G.R. Rao, *Ultralayered Co3O4 for High-Performance Supercapacitor Applications.* The Journal of Physical Chemistry C, 2011. **115**(31): p. 15646-15654.